Research paper

Low-thrust de-orbiting from Low Earth Orbit through natural perturbations

S. Huang [a,1], C. Colombo [a,2,*], E.M. Alessi [b,3], Y. Wang [a,4], Z. Hou [c,5]

[a] *Politecnico di Milano, Italy*
[b] *Consiglio Nazionale delle Ricerche, Italy*
[c] *Sun Yat-Sen University, China*

ARTICLE INFO

ABSTRACT

This paper investigates two strategies that exploit low-thrust propulsion and natural effects for the complete de-orbiting of spacecraft from a Low Earth Orbit (LEO). The first strategy aims to actively lower the perigee altitude by low-thrust propulsion to achieve passive drag-induced re-entry. The second strategy aims to actively move the spacecraft by low-thrust propulsion to reach a specific condition that can provoke passive orbital decay by means of the coupled effect of natural perturbations. For each strategy, a sub-time-optimal closed-loop steering law, which is proved to be stable, is designed with the Lyapunov method. Then a set of maps that show the costs of de-orbiting from LEO (i.e., the Δv-budget and de-orbiting time) are plotted as a function of the initial conditions for the two strategies. In this way, the feasible initial conditions to apply the two strategies are identified by comparing the Δv-budget. Before plotting the maps, the averaged low-thrust motion is derived, to reduce the computational load for the orbital propagation of low-thrust motion.

1. Introduction

In the recent years, we are witnessing a tendency of launching large satellite constellations, which are composed of hundreds to thousands of satellites, to provide low-latency broadband Internet access from the Low Earth Orbit (LEO) region. With numerous satellites deployed in the already congested LEO region, a severe safety threat is posed to the space environment [1]. For no doubt, it is necessary to de-orbit LEO spacecraft at their End of Life (EoL), to keep the space clean and sustainably useable.

Due to the high specific impulse, the low-thrust technologies have become more and more popular for space missions. A pioneering work on the EoL disposal from LEO with low-thrust was carried out in Ref. [2], where two strategies were investigated: one was to lower the perigee altitude to the drag-dominated region to achieve drag-induced re-entry, and the other was to move spacecraft to the graveyard altitudes between 2000 and 2500 km that are rarely used because of the intense radiation. By comparing the Δv-budget between the two strategies (assuming that the perigee altitude was lowered to 250 km), it was recommended to use the former strategy for the initial altitudes

lower than 1250 km and the latter strategy for the initial altitudes higher than 1250 km. However, as the latter strategy makes spacecraft accumulating at the graveyard altitudes, a source of explosion and collisions will be posed. So, it would be desired to find an alternative strategy that can achieve de-orbiting from the middle- and high-altitude LEO region with a low Δv-budget.

With the development of materials and manufacturing technologies, more and more deployable devices, such as the drag and solar sail, drag balloon, and electrodynamic tether, have been considered in various space missions [3–6], including the passive de-orbiting through natural perturbations. Over the past years, considerable feasibility studies on passive de-orbiting devices have been performed, demonstrating that such devices can enhance the de-orbiting from high-altitude orbits, by exploiting the orbital resonances due to the coupled effect of the Earth oblateness and Solar Radiation Pressure (SRP) [7–11]. However, the successful implementation of passive de-orbiting devices can be achieved only if the conditions of orbital resonances are satisfied; otherwise it will take a long period of time to de-orbit [7,9]. In order to better exploit the orbital resonances, a strategy to move spacecraft

---

Nomenclature

Acronyms

CPU	Centre Processing Unit
EoL	End-of-Life
EoM	Equation of Motion
LEO	Low Earth Orbit
RAAN	Right Ascension of the Ascending Node
SRP	Solar Radiation Pressure
ToF	Time of Flight
TPBVP	Two-Point Boundary Value Problem

Constants

Apparent mean motion of the Sun $n_S \approx 2\pi/365.25$ rad/s
Earth gravitational parameter $\mu \approx 3.9860 \times 10^5$ km^3/s^2
Earth standard gravity $g_0 \approx 9.8066$ m/s^2
Earth second zonal harmonics $J_2 \approx 0.0011$
Earth mean equatorial radius $R_\oplus \approx 6378.16$ km

Symbol

t	Time, s
a	Semi-major axis, km
e	Eccentricity
i	Inclination, rad or deg
Ω	RAAN, rad or deg
ω	Argument of perigee, rad or deg
E	Eccentric anomaly, rad or deg
m	Spacecraft mass, kg
f	Magnitude of the low-thrust acceleration vector, km/s^2
f_r	Radial component of the low-thrust acceleration vector, km/s^2
f_θ	Transversal component of the low-thrust acceleration vector, km/s^2
f_h	Normal component of the low-thrust acceleration vector, km/s^2
α	In-plane steering angle, rad or deg
β	Out-of-plane steering angle, rad or deg
F	Thrust, N
I_{sp}	Specific impulse, s
h	Altitude, km
h_{tar}	Target perigee altitude, km
V	Lyapunov function
fun	Primitive function
x	Orbital elements to be averaged
Δv	Change in velocity, km/s^2
b	Fourier series coefficient
c_a, c_e, c_i	Auxiliary coefficients
n_1, n_2, n_3	Coefficients for the de-orbiting corridors

Superscript and Subscript

str1	Perigee decrease strategy
str2	De-orbiting corridor strategy
0	Initial
f	Final

On the basis of the review of the aforementioned de-orbiting techniques, this paper will consider two de-orbiting strategies that can completely de-orbit spacecraft from LEO: the strategy lowering the perigee altitude and the strategy applying the passive de-orbiting device, named *perigee decrease strategy* and *de-orbiting corridor strategy*, respectively. A general study of the active de-orbiting subject to the low-thrust effect and of the passive de-orbiting subject to the natural effects, i.e., the drag effect in the perigee decrease strategy and the coupled effect of the Earth oblateness and SRP in the de-orbiting corridor strategy, will be performed for de-orbiting from any initial locations in the LEO region.

In order to exploit the natural effects for passive de-orbiting, low-thrust trajectories, or steering laws, have to be first designed to reach the conditions of the natural effects. In the field of low-thrust trajectory optimisation, there are two general approaches: indirect methods and direct methods [14,15]. Indirect methods solve a Two-Point Boundary Value Problem by means of the shooting method. However, the optimal solutions are usually difficult to obtain for long-duration transfers because of the small convergence domain. Direct methods, on the other side, solve a parameter optimisation problem by Nonlinear Programming. Compared to indirect methods, direct methods have a larger convergence domain and thus are feasible to handle long-duration transfers. However, direct methods usually require a great computational effort due to the large number of optimisation variables. Alternatively, heuristic methods, which are orders of magnitude faster than indirect and direct methods [16], have also received some attention, although may lead to non- or sub-optimal solutions. A first category of heuristic methods is involved in blending the steering laws that can instantaneously optimise the time rates of change of orbital elements [17–21]. A second category of heuristic methods is based on the Lyapunov stationary theory, where a candidate Lyapunov function must be properly defined to ensure convergence. Ref. [22] proposed a Q-Law algorithm based on a Lyapunov candidate function Q, which was a proximity quotient to quantify the proximity of the osculating orbit to the target orbit. Then the divergence problem exhibited in Ref. [22] was addressed in Ref. [16] by introducing penalty functions. Ref. [23] used the Lyapunov method to solve planar transfer and rendezvous problems, where the candidate Lyapunov functions proposed were able to give rise to asymptotically stabilising steering laws. However, one drawback of the Lyapunov method is that there does not exist a well-defined method to select controller gains [24], and some researchers have to resort to stochastic methods, such as genetic algorithm [25,26], which in turn will increase the computational load. A third category of heuristic methods aim to design closed-loop steering laws which are analytically described in terms of orbital elements, to further reduce computational effort and for potential real-time onboard autonomous guidance. Ref. [27] proposed a closed-loop steering law which was able to simultaneously offsetting the instantaneous errors in orbital elements; an improvement of this steering law but focused on planar transfer can be found in Ref. [28]. Ref. [29] managed to derive the closed-loop sub-time-optimal and sub-fuel-optimal steering laws for Geosynchronous Orbit transfer by optimising two objective functions, which were properly constructed based on the instantaneous variations of orbit elements and the cumulative effects of thrust, separately. As a matter of fact, all aforementioned methods are usually not stand-alone but mixed in light of their respective strengths and drawbacks according to the specific problems to be addressed.

In this paper, we will use the Lyapunov method to design closed-loop steering laws, one for each strategy. If the steering laws are proved to be stable, then they will be promptly applied to all transfers in the LEO region, thus reducing the computational effort for the present mission analysis and design. In order to minimise the negative impact on the space environment, it would be desired to de-orbit spacecraft as fast as possible, and thus the steering laws will be designed to be time-optimal by minimising the time rates of change of the candidate

to the conditions of orbital resonances with impulsive thrust was investigated in Refs. [12,13], showing that the Δv-budget would increase with the required change in semi-major axis and inclination.
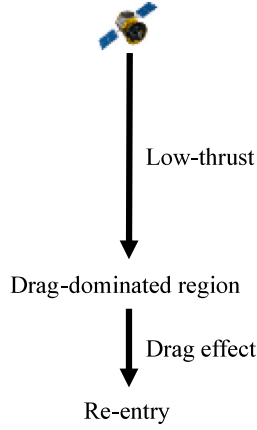
Fig. 1. Illustration of the perigee decrease strategy.

Fig. 2. Location of the six de-orbiting corridors, assuming $e = 0.001$ (blue: $n_1 = 1$, $n_2 = 1$, $n_3 = -1$; orange: $n_1 = 1$, $n_2 = -1$, $n_3 = -1$; yellow: $n_1 = 0$, $n_2 = 1$, $n_3 = -1$; purple: $n_1 = 0$, $n_2 = 1$, $n_3 = 1$; green: $n_1 = 1$, $n_2 = 1$, $n_3 = 1$; light blue: $n_1 = 1$, $n_2 = -1$, $n_3 = 1$). (For interpretation of the references to colour in this figure legend, the reader is referred to the web version of this article.)

Lyapunov functions. Then to evaluate the feasibility of the two strategies, a set of maps that show the costs of de-orbiting from LEO, i.e., the Δv-budget and de-orbiting time, will be plotted as a function of initial altitude and inclination, which are key drivers dominating the costs. Finally, following the work in Ref. [2] which is to compare the Δv-budget between two strategies, the feasible altitudes and inclinations to apply the two strategies will be identified. Before plotting the maps, to further reduce the computational load for the orbital propagation of low-thrust motion starting from all possible initial locations in the LEO region, the averaged low-thrust motion will be derived by using an orbital averaging technique. It has to be noted that the study scope of this paper is specified as follows.

(1) Throughout the de-orbiting process, the eccentricity is considered between 0 and 0.2.
(2) All initial inclinations are considered between 30 and 120 deg, not only because most of LEO missions are located in this range, but also for the reason that if out of this range, the Δv-budget of the de-orbiting corridor strategy will be too high to afford [12,13].

The remaining of this paper is organised as follows. Section 2 will give an overview of the two strategies. Section 3 will design the steering laws and prove the stability, following that the averaged low-thrust motion will be derived in Section 4. Finally in Section 5, the numerical simulations will be performed to validate the steering laws and averaged low-thrust motion, and the maps will be plotted.

2. Description of de-orbiting strategies

This section will give an overview of the two de-orbiting strategies.

2.1. Description of perigee decrease strategy

In the perigee decrease strategy, the low-thrust manoeuvres are performed to lower the perigee altitude to the drag-dominated region; after that the drag effect is strong enough to lower the apogee altitude until re-entry happens [2]. An illustration of the perigee decrease strategy is given in Fig. 1.

2.2. Description of de-orbiting corridor strategy

A mapping of the LEO region was obtained in Ref. [30], revealing the existence of the specific initial conditions in semi-major axis, eccentricity, and inclination that can lead to orbital decay beyond the drag-dominated region. As a matter of fact, the decay, which lowers the perigee altitude, is caused by the increase in eccentricity. Such
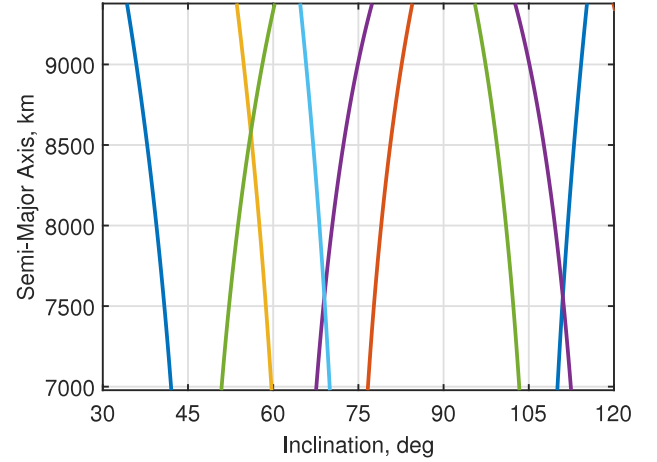
behaviour is mainly due to the coupled effect of the Earth oblateness and SRP, provided a large enough area-to-mass ratio. In principle, if the initial conditions for the decay are satisfied, then driven by the coupled effect, the decay will either follow the libration curves or the hyperbolic curves associated with the hyperbolic equilibrium points [11,31,32]. Hereinafter, the initial conditions that can provoke the natural decay in this way are referred to as the de-orbiting corridors [13].

In the LEO region, the location of the de-orbiting corridors can be approximated as a resonant condition which has six different forms [11]:

$$\left(\frac{d\Omega}{dt}\right)_{J_2} \pm \left(\frac{d\omega}{dt}\right)_{J_2} \pm n_S = 0, \quad \left(\frac{d\omega}{dt}\right)_{J_2} \pm n_S = 0 \tag{1}$$

where $(d\Omega/dt)_{J_2}$ and $(d\omega/dt)_{J_2}$ are the time rates of change of the Right Ascension of the Ascending Node (RAAN) Ω and of the argument of perigee ω, respectively, due to the secular effects of the Earth second zonal harmonics J_2, and n_S is the apparent mean motion of the Sun measured on the ecliptic plane. By substituting [33, Sec.9.6.1]

$$\left(\frac{d\Omega}{dt}\right)_{J_2} = -\frac{3\sqrt{\mu}R_\oplus^2 J_2}{2a^{7/2}\left(1-e^2\right)^2}\cos i \tag{2a}$$

$$\left(\frac{d\omega}{dt}\right)_{J_2} = \frac{3\sqrt{\mu}R_\oplus^2 J_2}{4a^{7/2}\left(1-e^2\right)^2}\left(4 - 5\sin^2 i\right) \tag{2b}$$

into Eq. (1), where a is the semi-major axis, e is the eccentricity, i is the inclination, μ is the Earth gravitational parameter, and $R_\oplus$ is the Earth mean equatorial radius, the location of the de-orbiting corridors can be described in terms of

$$\frac{3\sqrt{\mu}J_2 R_\oplus^2}{4a^{7/2}\left(1-e^2\right)^2}\left(5n_2\cos^2 i - 2n_1\cos i - n_2\right) + n_3 n_S = 0 \tag{3}$$

where $n_1 = (0, 1)$, $n_2 = \pm 1$, and $n_3 = \pm 1$ are the coefficients in front of $(d\Omega/dt)_{J_2}$, $(d\omega/dt)_{J_2}$, and n_S, respectively, that correspond to the six de-orbiting corridors. Fig. 2 shows the location of the de-orbiting corridors as a function of semi-major axis and inclination, assuming an eccentricity of 0.001.

In the de-orbiting corridor strategy, the low-thrust manoeuvres are performed to move the spacecraft to a target de-orbiting corridor that is closest to it, and then the passive de-orbiting device is deployed to artificially increase the area-to-mass ratio to enhance the subsequent orbital decay. It has to be noted that the decay beyond the drag-dominated region is mainly due to the coupled effect of the Earth
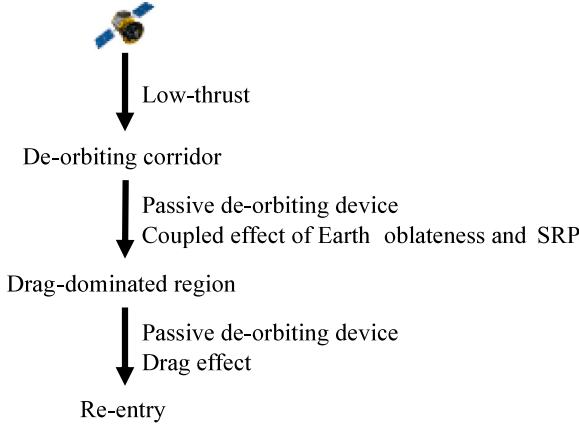
Fig. 3. Illustration of the de-orbiting corridor strategy.

Table 1

Values of $\left|\psi^{\text{str2}}\right|_{t=t_0}$ for the six de-orbiting corridors, taking as example an OneWeb satellite.

De-orbiting corridor	$\left\|\psi^{\text{str2}}\right\|_{t=t_0}$, $\times 10^{-6}$ rad/s
$n_1 = 1,\ n_2 = +1,\ n_3 = -1$	0.7862
$n_1 = 1,\ n_2 = -1,\ n_3 = -1$	0.3073
$n_1 = 0,\ n_2 = +1,\ n_3 = -1$	0.7459
$n_1 = 0,\ n_2 = +1,\ n_3 = +1$	0.3477
$n_1 = 1,\ n_2 = +1,\ n_3 = +1$	0.3880
$n_1 = 1,\ n_2 = -1,\ n_3 = +1$	0.7055

oblateness and SRP, while the decay within the drag-dominated region is mainly due to the drag effect, with the passive de-orbiting device acting as a drag sail. An illustration of the de-orbiting corridor strategy is given in Fig. 3.

Here the target de-orbiting corridor is chosen as the one needing the minimum effort, i.e., fuel consumption and travel time, to reach, and it can be found in the following way. From Eq. (3), we define

$$\left|\psi^{\text{str2}}\right|_{t=t_0} = \left| \frac{3\sqrt{\mu} J_2 R_\oplus^2}{4 a^{7/2} \left(1 - e^2\right)^2} \left(5 n_2 \cos^2 i - 2 n_1 \cos i - n_2\right)\Big|_{t=t_0} + n_3 n_S \right| \quad (4)$$

to quantitatively evaluate the effort to be made to reach the six de-orbiting corridors for a spacecraft whose initial state is given, where |∘| returns the absolute value of the generic variable ∘. Accordingly, the target de-orbiting corridor is the one having the minimum value of $\left|\psi^{\text{str2}}\right|_{t=t_0}$. Take as example an OneWeb satellite with the initial state of $a_0 = \left(1200 + R_\oplus\right)$ km, $e_0 = 0.001$, and $i_0 = 87.9$ deg [34]. Table 1 presents the values of $\left|\psi^{\text{str2}}\right|_{t=t_0}$ for the six de-orbiting corridors, and we can see the de-orbiting corridor that is closest to the OneWeb satellite is represented by $n_1 = 1$, $n_2 = -1$, and $n_3 = -1$. Such a way to find the target de-orbiting corridor is consistent with the logic of steering law design that will be presented in Section 3.2, where the candidate Lyapunov function to be sent to zero is defined as the square of $\left|\psi^{\text{str2}}\right|$. Fig. 4 shows the relative position between the OneWeb satellite and its target de-orbiting corridor indicated by the grey surface, and it can be seen that the main effort of the low-thrust manoeuvres is to drive the semi-major axis and inclination to approach the grey surface, i.e., the target de-orbiting corridor. In principle, the closer the initial semi-major axis and inclination to the target de-orbiting corridor, the less the effort will be needed.

3. Steering law design

As depicted in Section 2, for the purpose of exploiting the natural perturbations, the spacecraft has to be first moved to the drag-dominated region or de-orbiting corridor, i.e., the terminal condition
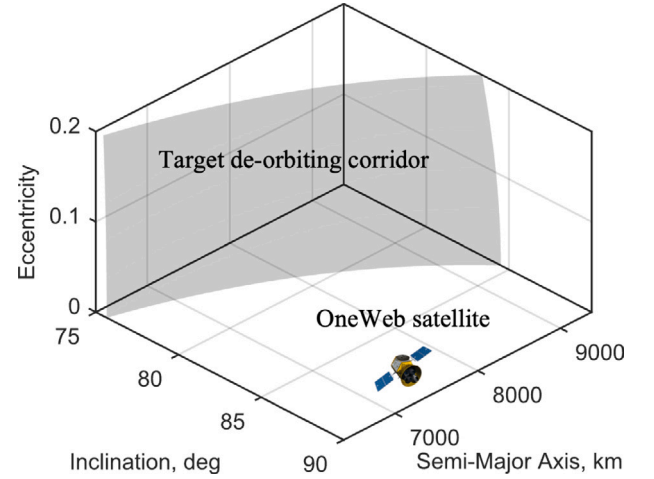

Fig. 4. Illustration of the relative position between the OneWeb satellite and its target de-orbiting corridor (grey surface).

of low-thrust transfer. This section will design the steering laws for the two de-orbiting strategies by using the Lyapunov method and will prove the stability of the steering laws.

3.1. Low-thrust dynamics model

For a spacecraft subject to the low-thrust effect, the Equations of Motion (EoMs) can be stated in the Gauss form as [35, Sec. 2.3]

$$\frac{\mathrm{d}a}{\mathrm{d}t} = \sqrt{\frac{a^3}{\mu}} \frac{2}{1 - e \cos E} \left(e \sin E f_r + \sqrt{1 - e^2} f_\theta \right) \quad (5a)$$

$$\frac{\mathrm{d}e}{\mathrm{d}t} = \sqrt{\frac{a\left(1 - e^2\right)}{\mu}} \frac{1}{1 - e \cos E} \left[\sqrt{1 - e^2} \sin E f_r \right. \\ \left. + \left(2 \cos E - e - e \cos^2 E\right) f_\theta \right] \quad (5b)$$

$$\frac{\mathrm{d}i}{\mathrm{d}t} = \sqrt{\frac{a}{\mu}} \left(\frac{\cos E - e}{\sqrt{1 - e^2}} \cos \omega - \sin E \sin \omega \right) f_h \quad (5c)$$

$$\frac{\mathrm{d}\Omega}{\mathrm{d}t} = \sqrt{\frac{a}{\mu}} \frac{1}{\sin i} \left(\frac{\cos E - e}{\sqrt{1 - e^2}} \sin \omega + \sin E \cos \omega \right) f_h \quad (5d)$$

$$\frac{\mathrm{d}\omega}{\mathrm{d}t} = \sqrt{\frac{a}{\mu}} \frac{1}{e\left(1 - e \cos E\right)} \left[\sqrt{1 - e^2}\left(e - \cos E\right) f_r \right. \\ \left. + \left(2 - e^2 - e \cos E\right) \sin E f_\theta \right] - \frac{\mathrm{d}\Omega}{\mathrm{d}t} \cos i \quad (5e)$$

$$\frac{\mathrm{d}E}{\mathrm{d}t} \approx \sqrt{\frac{\mu}{a^3}} \frac{1}{1 - e \cos E} \quad (5f)$$

where the low-thrust effect on $\mathrm{d}E/\mathrm{d}t$ is neglected because the low-thrust acceleration is very small compared to the Earth gravitational acceleration [36].

In the preceding equations, f_r, f_θ, and f_h are the radial, transversal, and normal components, respectively, of the low-thrust acceleration vector, given by

$$f_r = f \cos \beta \sin \alpha \quad (6a)$$

$$f_\theta = f \cos \beta \cos \alpha \quad (6b)$$

$$f_h = f \sin \beta \quad (6c)$$

where $f = F/m$ is the magnitude of the low-thrust acceleration vector, with F being the thrust and m being the spacecraft mass; α and β are the in-plane and out-of-plane steering angles, respectively, defined in Fig. 5, and the steering law design is to design the time histories of the steering angles. In this work, we consider a constant ejection propulsion model [37, Sec. 1.1], where the thrust F and the specific impulse I_{sp}
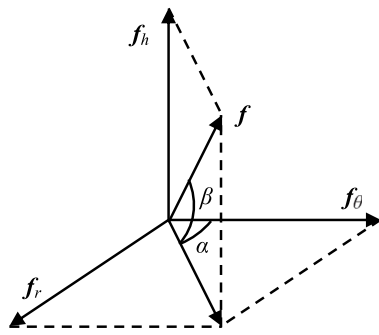
Fig. 5. Definition of steering angles.

Fig. 6. Evolution of the in-plane steering angle in Eq. (16) with eccentricity and eccentric anomaly.

are assumed constant. With this assumption, the spacecraft mass flow rate is also constant, given by [37, Sec. 1.1]

$$\frac{\mathrm{d}m}{\mathrm{d}t} = -\frac{F}{g_0 I_{\mathrm{sp}}} \tag{7}$$

where g_0 is the Earth standard gravity.

It is of note that the Gauss equations are singular for equatorial orbits (see Eq. (5d)) and for circular orbits (see Eq. (5e)). In this work, the singularity of equatorial orbits can be avoided because the inclination studied ranges from 30 to 120 deg, while the singularity of circular orbits will arise in the numerical simulations for orbital propagation. In the case of singularity, a set of non-singular orbital elements $(a,\ e_x,\ e_y,\ i,\ \Omega,\ L)$ can be used for orbital propagation computation; the conversion between classical and non-singular orbital elements are [33, Sec. 2.4.3]

$$e_x = e \cos \omega \tag{8a}$$

$$e_y = e \sin \omega \tag{8b}$$

$$L = \omega + E \tag{8c}$$

$$e = \sqrt{e_x^2 + e_y^2} \tag{9a}$$

$$\omega = \tan^{-1} \frac{e_y}{e_x} \tag{9b}$$

$$E = L - \omega \tag{9c}$$

Moreover, the steering laws proposed, the design of which will be presented in Sections 3.2 and 3.3, are also valid for circular orbits, although they are given in the form of classical orbital elements. For the perigee decrease strategy, the eccentricity will continuously grow, thus able to escape from the singularity status once exerting the thrust force. For the de-orbiting corridor strategy, the steering law (see Eq. (32)) can also be expressed as a function of the non-singular orbital element L, thus valid for circular orbits.

3.2. Steering law design for perigee decrease strategy

Given the aim to lower the perigee altitude, the terminal condition of low-thrust transfer for the perigee decrease strategy is

$$\psi^{\mathrm{str1}}\Big|_{t=t_f} = a(1-e)\Big|_{t=t_f} - (h_{\mathrm{tar}} + R_\oplus) = 0 \tag{10}$$

where $a(1-e)$ represents the perigee radius and h_{tar} is the target perigee altitude.

Here we define the candidate Lyapunov function for the perigee decrease strategy as

$$\begin{aligned} V^{\mathrm{str1}} &= \psi^{\mathrm{str1}} \\ &= a(1-e) - (h_{\mathrm{tar}} + R_\oplus) \end{aligned} \tag{11}$$

Accordingly, the time rate of change of V^{str1} is

$$\frac{\mathrm{d}V^{\mathrm{str1}}}{\mathrm{d}t} = \frac{\mathrm{d}a}{\mathrm{d}t}(1-e) - a\frac{\mathrm{d}e}{\mathrm{d}t} \tag{12}$$
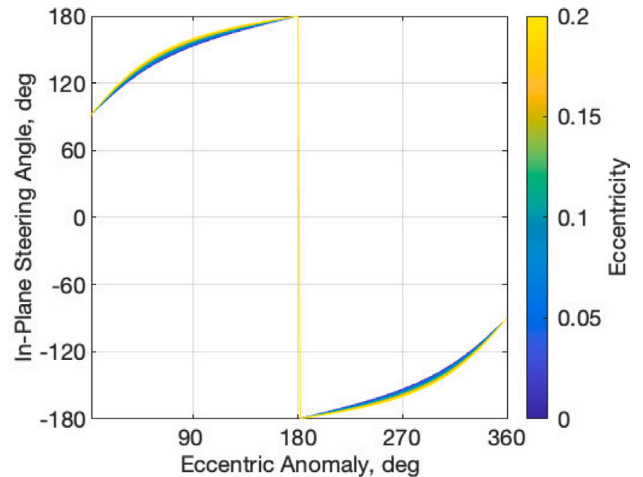
Recall from Eqs. (5a) and (5b) that $\mathrm{d}a/\mathrm{d}t$ and $\mathrm{d}e/\mathrm{d}t$ are functions of f_r and f_θ. So, $\mathrm{d}V^{\mathrm{str1}}/\mathrm{d}t$ is governed by the in-plane low-thrust acceleration components f_r and f_θ only, while the out-of-plane low-thrust acceleration component f_h can be set to zero and from Eq. (6c), $\beta = 0$. Thus, the low-thrust acceleration components for the perigee decrease strategy are written in the form of

$$f_r^{\mathrm{str1}} = f \sin \alpha \tag{13a}$$

$$f_\theta^{\mathrm{str1}} = f \cos \alpha \tag{13b}$$

$$f_h^{\mathrm{str1}} = 0 \tag{13c}$$

Then substituting Eqs. (5a) and (5b) into Eq. (12) and replacing the low-thrust acceleration components with Eq. (13), $\mathrm{d}V^{\mathrm{str1}}/\mathrm{d}t$ becomes

$$\begin{aligned} \frac{\mathrm{d}V^{\mathrm{str1}}}{\mathrm{d}t} = f\sqrt{\frac{\mu}{a^3}}\frac{1}{1-e\cos E} \Big\{ &-(1-e)^2 \sin E \sin \alpha \\ &+ \sqrt{1-e^2}\left[2(1-\cos E) - e\sin^2 E\right]\cos \alpha \Big\} \end{aligned} \tag{14}$$

It is clear from the definition of the candidate Lyapunov function in Eq. (11) that V^{str1} is zero at the final state and positive elsewhere. So, the goal of the low-thrust transfer is to drive V^{str1} to zero. In this work we choose the in-plane steering law that can minimise V^{str1} at the fastest rate, to send V^{str1} to zero as quickly as possible at any instant. By solving

$$\begin{cases} \dfrac{\partial(\mathrm{d}V^{\mathrm{str1}}/\mathrm{d}t)}{\partial \alpha} = 0 \\ \dfrac{\partial^2(\mathrm{d}V^{\mathrm{str1}}/\mathrm{d}t)}{\partial \alpha^2} \geq 0 \end{cases} \tag{15}$$

we get

$$\sin \alpha = \frac{(1-e)^2 \sin E}{\sqrt{(1-e)^4 \sin^2 E + (1-e^2)\left[2(1-\cos E) - e\sin^2 E\right]}} \tag{16a}$$

$$\cos \alpha = -\frac{\sqrt{1-e^2}\left[2(1-\cos E) - e\sin^2 E\right]}{\sqrt{(1-e)^4 \sin^2 E + (1-e^2)\left[2(1-\cos E) - e\sin^2 E\right]}} \tag{16b}$$

Fig. 6 shows the evolution of the in-plane steering angle in Eq. (16) with eccentricity and eccentric anomaly. It is observed from the plot that low values of e have little influence on α.

However, if using the in-plane steering law in Eq. (16), the EoMs will be in a complicated fashion, thus making it difficult to derive the averaged EoMs, which will be presented in Section 4.2. To address this problem, on the basis of the sensitivity analysis aforementioned, we

modify the in-plane steering law in Eq. (16) by setting $e = 0$:

$$\sin \alpha = \frac{\sin E}{\sqrt{\sin^2 E + 4(1 - \cos E)^2}} \tag{17a}$$

$$\cos \alpha = -\frac{2(1 - \cos E)}{\sqrt{\sin^2 E + 4(1 - \cos E)^2}} \tag{17b}$$

Finally, substituting Eq. (17) into Eq. (13), the low-thrust acceleration components for the perigee decrease strategy are

$$f_r^{\text{str1}} = f \frac{\sin E}{\sqrt{\sin^2 E + 4(1 - \cos E)^2}} \tag{18a}$$

$$f_\theta^{\text{str1}} = -f \frac{2(1 - \cos E)}{\sqrt{\sin^2 E + 4(1 - \cos E)^2}} \tag{18b}$$

$$f_h^{\text{str1}} = 0 \tag{18c}$$

Proposition 1. *Let a spacecraft be in the LEO region where $e \in [0, 0.2]$ and $i \in [30, 120]$ deg. If using the steering law in Eq. (17), all solutions governed by the dynamics model described in Section 3.1 will converge to any predefined target perigee altitude.*

Proof. By substituting Eq. (17) into Eq. (14), we get

$$\frac{\mathrm{d}V^{\text{str1}}}{\mathrm{d}t} = -f\sqrt{\frac{\mu}{a^3}} \frac{1}{1 - e\cos E}$$
$$\times \frac{(1 - e)^2 \sin^2 E + 2\sqrt{1 - e^2}(1 - \cos E)\left[2(1 - e\cos E) - e\sin^2 E\right]}{\sqrt{\sin^2 E + 4(1 - \cos E)^2}}$$

where the low-thrust acceleration magnitude $f > 0$, and

$$\sqrt{\frac{\mu}{a^3}} \frac{1}{1 - e\cos E} > 0$$
$$\sqrt{\sin^2 E + 4(1 - \cos E)^2} \geq 0$$

Because

$$(1 - e)^2 \sin^2 E \geq 0$$
$$2\sqrt{1 - e^2}(1 - \cos E) \geq 0$$
$$2(1 - e\cos E) - e\sin^2 E = 2(1 - e) + e(1 - \cos E)^2 > 0$$

there is

$$(1 - e)^2 \sin^2 E + 2\sqrt{1 - e^2}(1 - \cos E)\left[2(1 - e\cos E) - e\sin^2 E\right] \geq 0$$

Thus, $\mathrm{d}V^{\text{str1}}/\mathrm{d}t \leq 0$, where the equal sign does not hold indefinitely as E changes over time. So, V^{str1} always converges to zero. $\square$

3.3. Steering law design for de-orbiting corridor strategy

Given the aim to reach the target de-orbiting corridor, the terminal condition of low-thrust transfer for the de-orbiting corridor strategy is

$$\psi^{\text{str2}}\big|_{t=t_f} = \frac{3\sqrt{\mu}J_2 R_\oplus^2}{4a^{7/2}(1 - e^2)^2}\left(5n_2\cos^2 i - 2n_1\cos i - n_2\right)\bigg|_{t=t_f} + n_3 n_S = 0 \tag{19}$$

Here we define the candidate Lyapunov function for the de-orbiting corridor strategy as

$$V^{\text{str2}} = \left(\psi^{\text{str2}}\right)^2$$
$$= \left[\frac{3\sqrt{\mu}J_2 R_\oplus^2}{4a^{7/2}(1 - e^2)^2}\left(5n_2\cos^2 i - 2n_1\cos i - n_2\right) + n_3 n_S\right]^2 \tag{20}$$

Accordingly, the time rate of change of V^{str2} is

$$\frac{\mathrm{d}V^{\text{str2}}}{\mathrm{d}t} = \psi^{\text{str2}} \frac{3\sqrt{\mu}J_2 R_\oplus^2}{4a^{9/2}(1 - e^2)^3}\left[c_a(1 - e^2)\frac{\mathrm{d}a}{\mathrm{d}t} + 2c_e ae\frac{\mathrm{d}e}{\mathrm{d}t} + 2c_i a(1 - e^2)\frac{\mathrm{d}i}{\mathrm{d}t}\right] \tag{21}$$

where c_a, c_e, and c_i are functions of i:

$$c_a = -7\left(5n_2\cos^2 i - 2n_1\cos i - n_2\right) \tag{22a}$$

$$c_e = 4\left(5n_2\cos^2 i - 2n_1\cos i - n_2\right) \tag{22b}$$

$$c_i = 2n_1\sin i - 5n_2\sin 2i \tag{22c}$$

In the following we will perform the steering law design via two steps: first, selecting a proper in-plane steering law which can efficiently change a; second, designing an out-of-plane steering law which can drive the out-of-plane orbital element i, together with the in-plane orbital elements a and e, to reach the terminal condition as fast as possible.

There are two widely used in-plane steering laws that can efficiently change a: the transversal thrusting and the tangential thrusting; the latter is the optimal steering law to change a [38]. They are separately given by [35,39, Sec.2.4.2]

$$(\sin \alpha)_{\text{tra}} = 0 \tag{23a}$$

$$(\cos \alpha)_{\text{tra}} = \pm 1 \tag{23b}$$

$$(\sin \alpha)_{\text{tan}} = \pm\frac{e\sin E}{\sqrt{1 - e^2\cos^2 E}} \tag{24a}$$

$$(\cos \alpha)_{\text{tan}} = \pm\frac{\sqrt{1 - e^2}}{\sqrt{1 - e^2\cos^2 E}} \tag{24b}$$

where the sign $+$ and $-$ represent the cases of semi-major increase and decrease, respectively.

In this work we adopt the transversal thrusting, and the reasons are as follows.

(1) Irrespective of the out-of-plane steering law, the time rates of change of a due to the tangential and transversal thrusting are almost the same for low values of e, with a ratio of

$$\left(\frac{\mathrm{d}a}{\mathrm{d}t}\right)_{\text{tra}} \bigg/ \left(\frac{\mathrm{d}a}{\mathrm{d}t}\right)_{\text{tan}} = \sqrt{\left(1 - e^2\right) / \left(1 - e^2\cos^2 E\right)} \tag{25}$$

which is greater than 0.9798 for $e \in [0, 0.2]$.
(2) Compared to the tangential thrusting, the EoMs due to the transversal thrusting are in a simpler fashion, making it easier to derive the averaged EoMs in Section 4.3.

When the transversal thrusting serves as the in-plane steering law, substituting Eq. (23) into Eq. (13), the low-thrust acceleration components for the de-orbiting corridor strategy can be written in the form of

$$f_r^{\text{str2}} = 0 \tag{26a}$$

$$f_\theta^{\text{str2}} = f\cos \beta \tag{26b}$$

$$f_h^{\text{str2}} = f\sin \beta \tag{26c}$$

where the signs of the low-thrust acceleration components will be determined by the out-of-plane steering law. Then substituting Eqs. (5a), (5b), and (5c) into Eq. (21) and replacing the low-thrust acceleration components with Eq. (26), $\mathrm{d}V^{\text{str2}}/\mathrm{d}t$ becomes

$$\frac{\mathrm{d}V^{\text{str2}}}{\mathrm{d}t} = \psi^{\text{str2}} f \frac{3J_2 R_\oplus^2}{2a^3(1 - e^2)^{5/2}}\left(c_\beta\cos \beta + s_\beta\sin \beta\right) \tag{27}$$

where

$$c_\beta = \frac{c_a(1 - e^2) + c_e e(2\cos E - e - e\cos^2 E)}{1 - e\cos E} \tag{28a}$$
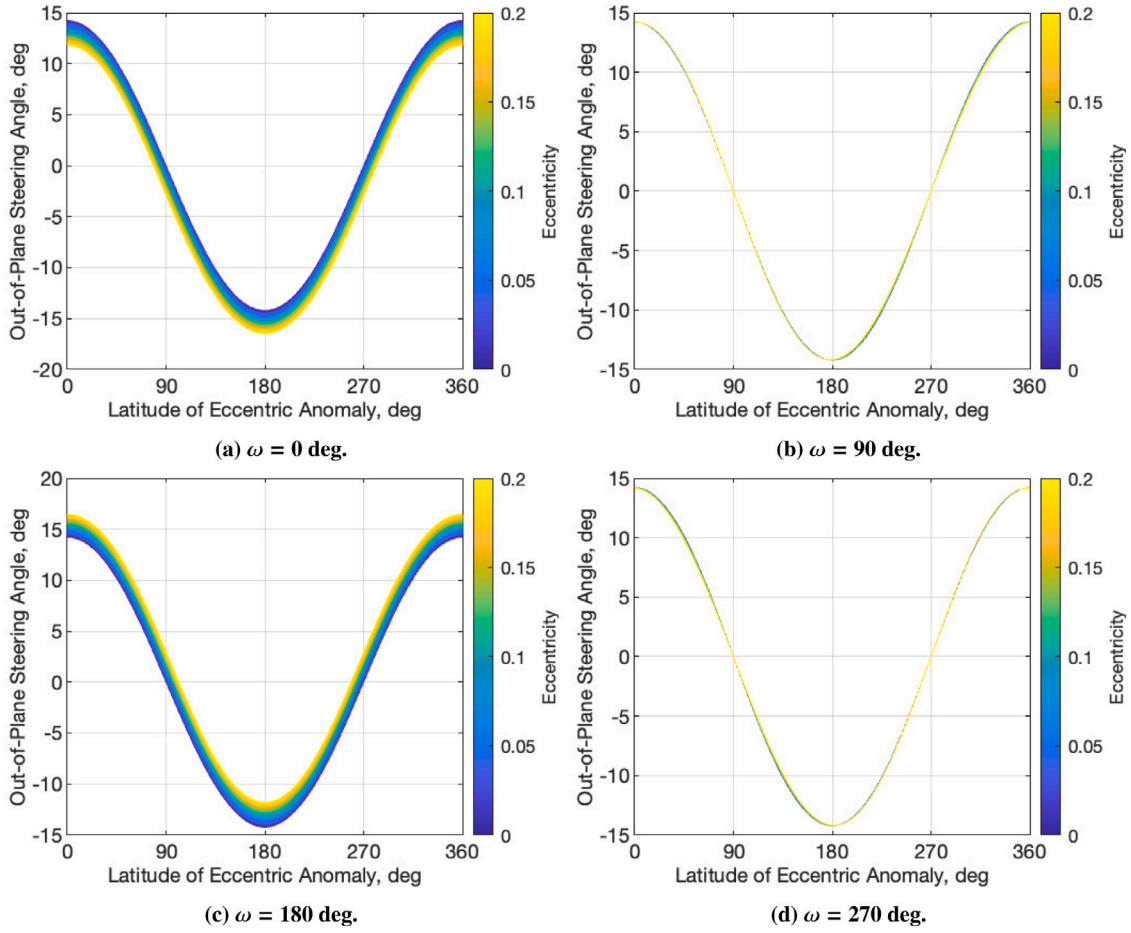
Fig. 7. Evolution of the out-of-plane steering angle in Eq. (30) with eccentricity and eccentric anomaly, assuming $i = 87.9$ deg.

$$s_\beta = c_i \left[(\cos E - e) \cos \omega - \sqrt{1 - e^2} \sin E \sin \omega \right] \quad (28b)$$

It is clear from the definition of the candidate Lyapunov function in Eq. (20) that V^{str2} is zero at the final state and positive elsewhere. So, the goal of the low-thrust transfer is to drive V^{str2} to zero. In this work we choose the out-of-plane steering law that can minimise V^{str2} at the fastest rate, to send V^{str2} to zero as quickly as possible at any instant. By solving

$$\begin{cases} \dfrac{\partial (dV^{str1}/dt)}{\partial \beta} = 0 \\ \dfrac{\partial^2 (dV^{str1}/dt)}{\partial \beta^2} \geq 0 \end{cases} \quad (29)$$

we get

$$\cos \beta = -\frac{\mathrm{sgn}_{\psi^{str2}} c_\beta}{\sqrt{c_\beta^2 + s_\beta^2}} \quad (30a)$$

$$\sin \beta = -\frac{\mathrm{sgn}_{\psi^{str2}} s_\beta}{\sqrt{c_\beta^2 + s_\beta^2}} \quad (30b)$$

where $\mathrm{sgn}_{\psi^{str2}}$ returns the sign of ψ^{str2}. Fig. 7 shows the evolution of the out-of-plane steering angle in Eq. (30) with eccentricity and the latitude of eccentric anomaly $(\omega + E)$ for different arguments of perigee, assuming an inclination of 87.9 deg. It is observed from the plot that low values of e have little influence on β; a similar phenomenon can be observed for other values of i.

Analogous to the perigee decrease strategy, for ease of deriving the averaged EoMs, which will be presented in Section 4.3, on the basis

of the sensitivity analysis aforementioned, we modify the out-of-plane steering law in Eq. (30) by setting $e = 0$:

$$\cos \beta = -\frac{\mathrm{sgn}_{\psi^{str2}} c_a}{\sqrt{c_a^2 + c_i^2 \cos^2 (\omega + E)}} \quad (31a)$$

$$\sin \beta = -\frac{\mathrm{sgn}_{\psi^{str2}} c_i \cos (\omega + E)}{\sqrt{c_a^2 + c_i^2 \cos^2 (\omega + E)}} \quad (31b)$$

Finally, substituting Eq. (31) into Eq. (26), the low-thrust acceleration components for the de-orbiting corridor strategy are

$$f_r^{str2} = 0 \quad (32a)$$

$$f_\theta^{str2} = -\mathrm{sgn}_{\psi^{str2}} f \frac{c_a}{\sqrt{c_a^2 + c_i^2 \cos^2 (\omega + E)}} \quad (32b)$$

$$f_h^{str2} = -\mathrm{sgn}_{\psi^{str2}} f \frac{c_i \cos (\omega + E)}{\sqrt{c_a^2 + c_i^2 \cos^2 (\omega + E)}} \quad (32c)$$

Proposition 2. *Let a spacecraft be in the LEO region where $e \in [0, 0.2]$ and $i \in [30, 120]$ deg. If using the steering laws in Eq. Eq. (23) and Eq. Eq. (31), all solutions governed by the dynamics model described in Section 3.1 converge to any predefined target de-orbiting corridor.*

Proof. By substituting Eq. (31) into Eq. (27), we get

$$\frac{dV^{str2}}{dt} = -\mathrm{sgn}_{\psi^{str2}} \psi^{str2} f \frac{3 J_2 R_\oplus^2}{2a^3 (1 - e^2)^{5/2}} \frac{c_\beta c_a + s_\beta c_i \cos (\omega + E)}{\sqrt{c_a^2 + c_i^2 \cos^2 (\omega + E)}}$$

In the preceding equation, $\mathrm{sgn}_{str2} \psi^{str2}$ is zero at the final state and positive elsewhere, the low-thrust acceleration magnitude $f > 0$, and

there are

$$\frac{3J_2 R_\oplus^2}{2a^3 \left(1 - e^2\right)^{5/2}} > 0$$

$$\sqrt{c_a^2 + c_i^2 \cos^2\left(\omega + E\right)} \geq 0$$

where the equal sign in the latter term holds only if both c_a and $\cos\left(\omega + E\right)$ are zero; however, $\cos\left(\omega + E\right)$ does not stay at zero indefinitely as E changes over time.

It is observed from Eq. (22) that $c_e = -(4/7)c_a$. Then using this relationship and replacing c_β and s_β with Eq. (28), after some manipulations, we have

$$c_\beta c_a + s_\beta c_i \cos\left(\omega + E\right) = c_a^2 \sigma + c_i^2 \varsigma$$

where

$$\sigma = \frac{3\left(1 - e^2\right) + 4\left(1 - e\cos E\right)^2}{7\left(1 - e\cos E\right)}$$

$$\varsigma = \left[\left(\cos E - e\right)\cos\omega - \sqrt{1 - e^2}\sin E \sin\omega\right]\cos\left(\omega + E\right)$$

Thus, to show that V^{str2} always converges to zero, it is necessary to show that

$$\begin{cases} \sigma + \dfrac{c_i^2}{c_a^2}\varsigma \geq 0 \text{ for } e \in [0,\ 0.2] \text{ and } i \in [30,\ 120] \text{ deg}, & \text{if } c_a \neq 0 \\ c_i^2 \varsigma \geq 0 \text{ for } e \in [0,\ 0.2] \text{ and } i \in [30,\ 120] \text{ deg}, & \text{if } c_a = 0 \end{cases}$$

where the equal sign does not hold indefinitely.

For σ, there are the following partial derivatives:

$$\frac{\partial \sigma}{\partial E} = \frac{e}{7}\left[4 - \frac{3\left(1 - e^2\right)}{\left(1 - e\cos E\right)^2}\right]\sin E$$

$$\frac{\partial^2 \sigma}{\partial E^2} = \frac{e}{7}\left[4\cos E - \frac{3\left(1 - e^2\right)\cos E}{\left(1 - e\cos E\right)^2} + \frac{6e\left(1 - e^2\right)\sin^2 E}{\left(1 - e\cos E\right)^3}\right]$$

By solving

$$\begin{cases} \dfrac{\partial \sigma}{\partial E} = 0 \\ \dfrac{\partial^2 \sigma}{\partial E^2} \geq 0 \end{cases}$$

we can get E that minimises σ for any e, given in the form of

$$\cos E = \frac{2 - \sqrt{3\left(1 - e^2\right)}}{2e}$$

Then substituting the preceding equation into the expression of σ, we have

$$\min_E \sigma = \frac{4\sqrt{3\left(1 - e^2\right)}}{7}$$

which monotonically decreases with e, and therefore

$$\sigma_{\min} = \min_{e,\ E} \sigma = 0.9697, \quad e \in [0,\ 0.2]$$

For ς, there are the following partial derivatives:

$$\frac{\partial \varsigma}{\partial \omega} = \frac{1}{2}\left[\left(\sqrt{1 - e^2} - 1\right)\right.$$
$$\left. \times \sin 2\omega - \left(\sqrt{1 - e^2} + 1\right)\sin\left(2\omega + 2E\right) + 2e\sin\left(2\omega + E\right)\right]$$

$$\frac{\partial \varsigma}{\partial E} = \left[\left(e - \cos E\right)\cos\omega + \sqrt{1 - e^2}\sin\omega\sin E\right]\sin\left(\omega + E\right)$$
$$- \left(\cos\omega\sin E + \sqrt{1 - e^2}\sin\omega\cos E\right)\cos\left(\omega + E\right)$$

$$\frac{\partial^2 \varsigma}{\partial \omega \partial E} = e\cos\left(2\omega + E\right) - \left(1 + \sqrt{1 - e^2}\right)\cos\left(2\omega + 2E\right)$$

Table 2
Minimum value of c_i^2/c_a^2 for $i \in [30,\ 120]$ deg.

De-orbiting corridor	$(c_i^2/c_a^2)_{\min}$
$n_1 = 1,\ n_2 = +1,\ n_3 = -1$	0.1492
$n_1 = 1,\ n_2 = -1,\ n_3 = -1$	0.0601
$n_1 = 0,\ n_2 = +1,\ n_3 = -1$	0.0980
$n_1 = 0,\ n_2 = +1,\ n_3 = +1$	0.0980
$n_1 = 1,\ n_2 = +1,\ n_3 = +1$	0.1492
$n_1 = 1,\ n_2 = -1,\ n_3 = +1$	0.0601

By solving

$$\begin{cases} \dfrac{\partial \varsigma}{\partial \omega} = 0 \\ \dfrac{\partial \varsigma}{\partial E} = 0 \\ \dfrac{\partial^2 \varsigma}{\partial \omega \partial E} \geq 0 \end{cases}$$

we can get ω and E that minimise ς for any e:

$$\omega = \frac{1}{2}\tan^{-1}\frac{\sqrt{1 - e^2}}{e} + \frac{3\pi}{4}$$
$$E = \frac{\pi}{2}$$

Then substituting the preceding equation into the expression of ς, we have

$$\min_{\omega,\ E}\varsigma = \frac{\sqrt{1 - e^2} - 1}{2}$$

which monotonically decreases with e, and therefore

$$\varsigma_{\min} = \min_{e,\ \omega,\ E}\varsigma = -0.0101, \quad e \in [0,\ 0.2]$$

For the case $c_a \neq 0$, because c_a and c_i are functions of i, we can compute the minimum value of c_i^2/c_a^2 for the six de-orbiting corridors, considering $i \in [30,\ 120]$ deg, as presented in Table 2. For all the de-orbiting corridors, there is

$$\sigma_{\min} + \left(\frac{c_i^2}{c_a^2}\right)_{\min}\varsigma_{\min} > 0, \quad e \in [0,\ 0.2]$$

Thus, V^{str2} always converges to zero if $c_a \neq 0$.

For the case $c_a = 0$, because $\varsigma_{\min} < 0$, there is

$$(c_i^2)_{\min}\varsigma_{\min} \leq 0$$

Thus, V^{str2} cannot converge to zero if $c_a = 0$. For the six de-orbiting corridors, the values of i that result in a zero c_a are (in degrees): 46.378, 63.435, 73.148, 106.852, and 116.565. Therefore, to guarantee that V^{str2} always converges to zero, the initial inclination must be specified to be outside of a small region surrounding these values. □

4. Averaged low-thrust equations of motion

In Section 5 we will carry out the de-orbiting mapping by propagating a series of initial conditions over the entire LEO region. In order to reduce the computational load for the orbital propagation of low-thrust motion, the averaged EoMs subject to the steering laws proposed will be derived with the orbital averaging technique.

4.1. Orbital averaging technique

Due to the fact that the low-thrust acceleration is small, typically on the order of $10^{-4}g_0$ or less [40], all orbital elements except E can be assumed constant within a single revolution. Let x denote any of the orbital elements to be averaged, i.e. $x \in (a,\ e,\ i,\ \Omega,\ \omega)$. If considering

a burning arc from E_{on} to E_{off}, the incremental change in x over one revolution can be obtained by integrating its rate of change with E:

$$\Delta x = \int_{E_{on}}^{E_{off}} \frac{dx}{dE} dE \tag{33}$$
$$= fun_x \left(E_{off} \right) - fun_x \left(E_{on} \right)$$

where fun_x is the primitive function of dx/dE, which will be derived in Sections 4.2 and 4.3 for the perigee decrease and de-orbiting corridor strategies, respectively. This incremental change occurs during an orbital period of $T = 2\pi/n$, where $n = \sqrt{\mu/a^3}$ is the perturbed mean motion. The averaged time rates of change of x is therefore

$$\frac{d\tilde{x}}{dt} = \sqrt{\frac{\mu}{a^3}} \frac{\Delta x}{2\pi} \tag{34}$$

4.2. Primitive functions for perigee-decrease strategy

Governed by the steering law designed in Section 3.2, the rates of change of orbital elements with E for the perigee decrease strategy are

$$\left\{ \left(\frac{da}{dE} \right)^{str1}, \left(\frac{de}{dE} \right)^{str1}, \left(\frac{d\omega}{dE} \right)^{str1} \right\}^{\top}$$

$$= \frac{f}{\sqrt{\sin^2 E + 4(1 - \cos E)^2}}$$

$$\times \left\{ \begin{array}{c} \frac{2a^3}{\mu} \left[e \sin^2 E - 2\sqrt{1-e^2}(1-\cos E) \right] \\ \frac{a^2\sqrt{1-e^2}}{\mu} \left[\sqrt{1-e^2} \sin^2 E - 2\left(2\cos E - e - e\cos^2 E \right)(1-\cos E) \right] \\ \frac{a^2}{\mu e} \left[\sqrt{1-e^2}(e - \cos E) \sin E - 2\left(2 - e^2 - e\cos E \right) \sin E (1-\cos E) \right] \end{array} \right\} \tag{35}$$

Note that $(di/dE)^{str1} = (d\Omega/dE)^{str1} = 0$ because $f_h^{str1} = 0$.

Then carrying out the integration of Eq. (35), after some manipulations, the primitive functions for the perigee decrease strategy are derived as

$$fun_a^{str1} = \frac{2fa^3}{\mu} \left[\frac{\sqrt{2}}{3} e \cos \frac{E}{2} \sqrt{5 - 3\cos E} \right. $$
$$\left. - \frac{4\sqrt{3}}{9} \left(3\sqrt{1-e^2} - 2e \right) \tan^{-1} \frac{\sqrt{5 - 3\cos E}}{\sqrt{6}\cos\frac{E}{2}} \right] \tag{36a}$$

$$fun_e^{str1} = \frac{fa^2\sqrt{1-e^2}}{\mu} \left[\frac{\sqrt{2}}{3} \left(\sqrt{1-e^2} + e - 4 + e\cos E \right) \right.$$
$$\times \cos \frac{E}{2} \sqrt{5 - 3\cos E}$$
$$\left. + \frac{8\sqrt{3}}{9} \left(\sqrt{1-e^2} + 3e - 1 \right) \tan^{-1} \frac{\sqrt{5 - 3\cos E}}{\sqrt{6}\cos\frac{E}{2}} \right] \tag{36b}$$

$$fun_\omega^{str1} = \frac{fa^2}{\mu e} \left[\frac{\sqrt{2}}{3} \left(\sqrt{1-e^2} + 2e^2 + 2e - 4 + e\cos E \right) \sin \frac{E}{2} \sqrt{5 - 3\cos E} \right.$$
$$\left. - \frac{2\sqrt{3}}{9} \left(\sqrt{1-e^2}(4 - 3e) + 2e^2 + 3e - 4 \right) \tanh^{-1} \frac{\sqrt{6}\sin\frac{E}{2}}{\sqrt{5 - 3\cos E}} \right] \tag{36c}$$

where $\tan^{-1} \circ$ and $\tanh^{-1} \circ$ return the *four-quadrant* inverse tangent and the inverse hyperbolic tangent, respectively, of the generic variable $\circ$.

4.3. Primitive functions for de-orbiting corridor strategy

Governed by the steering law designed in Section 3.3, the rates of change of orbital elements with E for the de-orbiting corridor strategy are

$$\left\{ \left(\frac{da}{dE} \right)^{str2}, \left(\frac{de}{dE} \right)^{str2}, \left(\frac{di}{dE} \right)^{str2}, \left(\frac{d\Omega}{dE} \right)^{str2}, \left(\frac{d\omega}{dE} \right)^{str2} \right\}^{\top}$$

$$= \frac{-\text{sgn}_{\psi}^{str2} f}{\sqrt{c_a^2 + c_i^2 \cos^2(\omega + E)}}$$

$$\times \left\{ \begin{array}{c} \frac{2c_a a^3 \sqrt{1-e^2}}{\mu} \\ \frac{c_a a^2 \sqrt{1-e^2}}{\mu} \left(2\cos E - e - e\cos^2 E \right) \\ \frac{c_i a^2}{\mu} \left(\frac{\cos E - e}{\sqrt{1-e^2}} \cos\omega - \sin E \sin\omega \right)(1 - e\cos E)\cos(\omega + E) \\ \frac{c_i a^2}{\mu} \left(\frac{\cos E - e}{\sqrt{1-e^2}} \sin\omega + \sin E \cos\omega \right) \frac{1 - e\cos E}{\sin i} \cos(\omega + E) \\ \frac{c_a a^2}{\mu e} \left(2 - e^2 - e\cos E \right) \sin E \end{array} \right\}$$

$$+ \left\{ 0, \ 0, \ 0, \ 0, \ -\left(\frac{d\Omega}{dE} \right)^{str2} \cos i \right\}^{\top} \tag{37}$$

However, Eq. (37) cannot be analytically integrated. For the purpose of addressing this problem, observing that the term $\cos(\omega + E)$ is periodic, we expand the following term in Fourier series up to 8th-order before carrying out the integration:

$$\frac{1}{\sqrt{c_a^2 + c_i^2 \cos^2(\omega + E)}} \approx \frac{2}{\pi\sqrt{c_a^2 + c_i^2}} \sum_{k=0}^{4} b_k \cos[2k(\omega + E)] \tag{38}$$

where b_k ($k = 0$ to 4) are Fourier series coefficients, given in the form of

$$b_k = b_k^F \text{elliptic} F(\rho) + b_k^E \text{elliptic} E(\rho) \tag{39}$$

with b_k^F and b_k^E dependent on c_a and c_i, given in Appendix A. Here the reason to choose the 8th-order Fourier series expansion is for the sake of achieving good accuracy with a reasonable computational effort. For an 8th-order Fourier series expansion, there should have been 17 coefficients, among which only five coefficients, i.e., b_0 to b_4, are non-zero in the current problem.

In Eq. (39), the complete elliptic integrals of the first and second kinds [41, Sec. 1.5]

$$\text{elliptic} F(\rho) = \int_0^{\pi/2} \left(1 - \rho \sin^2 \varphi \right)^{-1/2} d\varphi \tag{40a}$$

$$\text{elliptic} E(\rho) = \int_0^{\pi/2} \left(1 - \rho \sin^2 \varphi \right)^{1/2} d\varphi \tag{40b}$$

are to be evaluated, where the modulus ρ is

$$\rho = \frac{c_i^2}{c_a^2 + c_i^2} \tag{41}$$

Then substituting Eq. (38) into Eq. (37) and carrying out the integration, after considerable manipulations, the primitive functions for

Table 3

Simulation parameters.

Parameter	Symbol	Value	Unit
Initial eccentricity	e_0	0.001	
Initial RAAN	Ω_0	0	rad
Initial argument of perigee	ω_0	1	rad
Initial eccentric anomaly	E_0	2	rad
Initial spacecraft mass	m_0	150	kg
Thrust	F	13.596	mN
Specific impulse	I_{sp}	1500	s
Drag coefficient	C_D	2.1	
Reflectivity coefficient	C_R	1	

the de-orbiting corridor strategy are derived as

$$
\left\{ fun_a^{str2}, \ fun_e^{str2}, \ fun_i^{str2}, \ fun_\Omega^{str2}, \ fun_\omega^{str2} \right\}^\top
$$

$$
= \frac{-\mathrm{sgn}_{\psi^{str2}} f}{\pi \mu \sqrt{c_a^2 + c_i^2}} \left\{ \begin{array}{l} \left[\sum_{k=0}^4 b_k \left(fun_k \right)_a \right] c_a a^3 \sqrt{1-e^2} \\[2mm] \left[\sum_{k=0}^4 b_k \left(fun_k \right)_e \right] c_a a^2 \sqrt{1-e^2} \\[2mm] \left[\sum_{k=0}^4 b_k \left(fun_k \right)_i \right] c_i a^2 \\[2mm] \left[\sum_{k=0}^4 b_k \left(fun_k \right)_\Omega \right] \dfrac{c_i a^2}{\sin i} \\[2mm] \left[\sum_{k=0}^4 b_k \left(fun_k \right)_\omega \right] \dfrac{c_a a^2}{e} \end{array} \right\} \tag{42}
$$

$$
+ \left\{ 0, \ 0, \ 0, \ 0, \ -fun_\Omega^{str2} \cos i \right\}^\top
$$

where $\left(fun_k \right)_x$ ($k = 0$ to 4 and $x \in (a, e, i, \Omega, \omega)$) are functions of e, ω, and E, given in Appendix.

5. Numerical simulations and discussion

In this section, the numerical simulations will be performed to validate the steering laws proposed and averaged low-thrust EoMs, and the de-orbiting mapping will be carried out to obtain the costs of de-orbiting from the LEO region and the feasible initial conditions of the two strategies. Table 3 gives the simulation parameters that are fixed for this work. Specifically, the initial eccentricity is a representative value for LEO missions; the initial RAAN, argument of perigee, and eccentric anomaly are randomly chosen because they have little impact on spacecraft de-orbiting behaviour; the initial spacecraft mass, the thrust, and the specific impulse are typical values for small-satellite missions. It is of note that the decrease and increase of the initial eccentricity will lengthen and shorten the time of re-entry, respectively, but the underlying re-entry mechanism is the same [31,32].

5.1. Numerical validations

In this part, a test transfer for an OneWeb-like satellite [34] will be presented to demonstrate the optimality of the steering laws proposed and the accuracy of the averaged low-thrust EoMs. Table 4 gives the simulation parameters, where the value of h_{tar} is taken from Ref. [2], such that the satellite can quickly re-enter. It is of note that although the validation is made for a specific orbit, the steering laws proposed are inherently sub-optimal within the study scope (i.e., $e \in [0, 0.2]$ and $i \in [30, 120]$ deg) because they can send the candidate Lyapunov function at the fastest rate and are proved to be stable, and the averaged EoMs can also be applied to any type of orbit within the study scope.

5.1.1. Validations for steering laws

With the aim to reduce the negative impact on the space environment as much as possible, the low-thrust transfer is desired to be time-optimal. Thus, we compare the Times of Flight (ToFs), which is

Table 4

Simulation parameters for the test transfer of an OneWeb-like satellite.

Parameter	Symbol	Value	Unit
Initial semi-major axis	a_0	$R_\oplus + 1200$	km
Initial inclination	i_0	87.9	deg
Target perigee altitude	h_{tar}	250	km

Table 5

Initial costates.

Initial costate	Value		Unit
	Perigee decrease strategy	De-orbiting corridor strategy	
$(\lambda_a)_0$	$+4.2662 \times 10^3$	$+4.7356 \times 10^3$	s/km
$(\lambda_e)_0$	-3.6820×10^7	-9.6343×10^4	s
$(\lambda_i)_0$	0	$+2.7379 \times 10^7$	s/rad
$(\lambda_\Omega)_0$	0	0	s/rad
$(\lambda_\omega)_0$	0	17.342	s/rad
$(\lambda_E)_0$	$+3.0386 \times 10^2$	15.063	s/rad
$(\lambda_m)_0$	$+3.0798 \times 10^4$	$+6.1801 \times 10^4$	s/kg

Table 6

Comparisons between closed- and open-loop steering laws.

Steering law	ToF, days	
	Perigee decrease strategy	De-orbiting corridor strategy
Closed-loop	56.392	108.577
Open-loop	56.105	108.576

the time of low-thrust transfer, between the present closed-loop steering laws and the time-optimal open-loop steering laws. In this work, the open-loop steering laws are obtained by the indirect method, where on the basis of the optimal control theory [42], the minimum-time optimisation problem is converted to a Two-Point Boundary Value Problem (TPBVP) and solved by the shooting method. Table 5 gives the initial costates of the open-loop steering laws for the two strategies. A detailed description of the time-optimal open-loop control law design and the derivation of initial costates is given in Appendix B.

Table 6 presents the comparisons of ToFs between closed- and open-loop steering laws for the two strategies. As indicated in the table, for both strategies, the ToFs of the closed-loop steering laws are very close to the optimal solutions.

5.1.2. Validations for averaged low-thrust equations of motion

In order to validate the accuracy of the averaged EoMs, we perform the numerical integration of the exact EoMs, i.e., Eq. (5), and the averaged EoMs and compare the results. In this work, the numerical integration is carried out with MATLAB R2020b running on a computer with Intel Core i7-8550U and 8 GB Random Access Memory; the Ordinary Differential Equation solver ode45 is applied, where the absolute and relative error tolerances are specified as 10^{-13}.

Tables 7 and 8 present the comparisons between exact and averaged EoMs for the perigee decrease and de-orbiting corridor strategies, respectively, in terms of the final states, ToF, and Centre Processing Unit (CPU) time. As indicated in the tables, the averaged EoMs can significantly reduce the CPU time while maintaining good accuracy.

Moreover, to estimate the limit of the accuracy of the assumption used in the orbital averaging technique, some additional simulations are performed with the consideration of different levels of thrust acceleration; recall that the assumption is keeping all orbital elements except for the eccentric anomaly as constant within every single revolution. Tables 9 and 10 present the errors of the final results for the averaged EoMs, considering several typical acceleration levels in low-thrust missions. It can be seen that all final results apart from the final argument of perigee can maintain good accuracy, where the comparatively large error in the final argument of perigee is caused by the small initial eccentricity.

Table 7

Comparison between exact and averaged EoMs for the perigee decrease strategy.

EoMs	a_f, km	e_f, $\times 10^{-2}$	ω_f, rad	m_f, kg	ToF, days	CPU time, s
Exact	6910.432	4.0847	−2.1275	145.496	56.4011	6.237
Averaged	6910.399	4.0843	−2.1515	145.496	56.4030	0.007

Table 8

Comparison between exact and averaged EoMs for the de-orbiting corridor strategy.

EoMs	a_f, km	e_f, $\times 10^{-4}$	i_f, deg	Ω_f, rad	ω_f, rad	m_f, kg	ToF, days	CPU time, s
Exact	9705.773	7.6915	86.515	0.3242	−2.4849	141.329	108.5776	5.770
Averaged	9705.759	8.3046	86.515	0.3242	−2.4589	141.329	108.5773	0.039

Table 9

Final errors introduced by the averaged EoMs for different levels of thrust acceleration for the perigee decrease strategy.

Thrust acceleration, km/s^2	ϵ_a, km	ϵ_e	ϵ_ω, rad	ϵ_m, kg	ϵ_{ToF}, days
1×10^{-7}	−0.0883	-1.2250×10^{-5}	−0.0261	-9.8608×10^{-4}	0.0112
1×10^{-6}	−0.2272	-3.1536×10^{-5}	−0.1983	−0.0028	0.0031
1×10^{-5}	−1.7555	-2.4360×10^{-4}	−0.4931	−0.0259	0.0029

Table 10

Final errors introduced by the averaged EoMs for different levels of thrust acceleration for the de-orbiting corridor strategy.

Thrust acceleration, km/s^2	ϵ_a, km	ϵ_e	ϵ_i, deg	ϵ_Ω, rad	ϵ_ω, rad.	ϵ_m, kg	ϵ_{ToF}, days
1×10^{-7}	+0.0177	$+2.7660 \times 10^{-5}$	$+1.1939 \times 10^{-4}$	5.8018×10^{-6}	−0.0463	-2.8160×10^{-5}	$+3.1963 \times 10^{-4}$
1×10^{-6}	+0.2247	-8.1869×10^{-5}	+0.0015	3.0545×10^{-5}	+0.6723	-3.6426×10^{-4}	$+4.1345 \times 10^{-4}$
1×10^{-5}	−1.6890	−0.0033	−0.0109	3.1416×10^{-4}	+0.6462	+0.0027	-3.0812×10^{-4}

5.2. De-orbiting mapping

In this part, a set of maps will be plotted to show the Δv-budget and de-orbiting time for the de-orbiting from different initial altitudes and inclinations, and then based on the maps, the feasible altitudes and inclinations to apply the two strategies will be identified. Here, the Δv-budget refers to the change in velocity of low-thrust transfer, and the de-orbiting time refers to the total time to de-orbit, including the time of low-thrust transfer, i.e., the ToF, and the time of passive de-orbiting subject to the natural perturbations until re-entry.

5.2.1. Force models and simulation settings

In the simulations for passive de-orbiting, the orbital propagator developed for the ReDSHIFT software tool [43,44] is applied. It considers:

(1) Earth zonal harmonics up to degree 5
(2) SRP with the cannonball model
(3) lunisolar perturbations
(4) atmospheric drag with the Jacchia–Roberts atmospheric density model, assuming an exospheric temperature of 1000 K and a variable solar flux at 2800 MHz

Ref. [45] has proven that the de-orbiting corridors considering the aforementioned force models persist under a high-fidelity not-averaged model accounting for shadows and other harmonics.

For the perigee decrease strategy, the area-to-mass ratio is set to 0.012 m^2/kg, which is an average value of the orbiting intact population [46]. For the de-orbiting corridor strategy, the area-to-mass ratios are set to 1 and 3 m^2/kg; the former is a feasible value achievable for small satellites [30], whereas the latter has a potential application for quick re-entry. For both strategies, the re-entry is assumed to happen whenever the perigee altitude is decreased to a demise value of 78 km.

Table 11 defines the grids of the initial altitude h_0 for both strategies, of the initial inclination i_0 for the de-orbiting corridor strategy, and of the target perigee altitude h_{tar} for the perigee decrease strategy. In the following simulations, the value of i_0 for the perigee decrease strategy, which has ignorable influence on the results compared to h_0 and h_{tar}, is fixed as 63.435 deg.
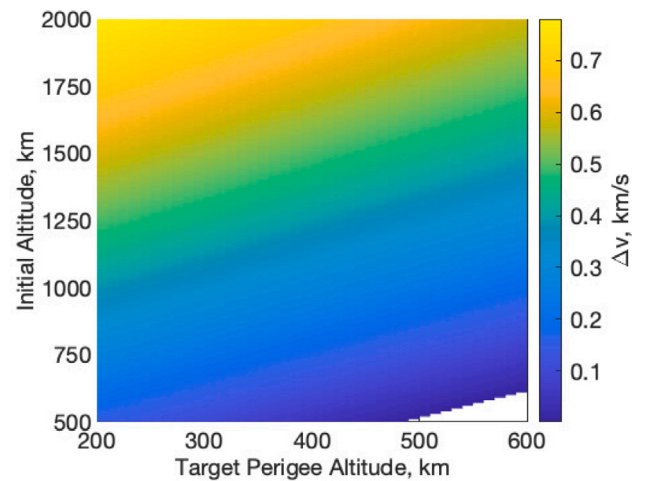

Fig. 8. Δv-budget for the perigee decrease strategy.
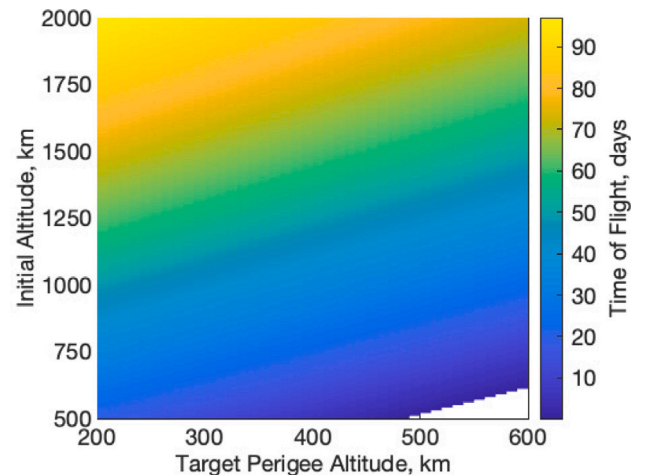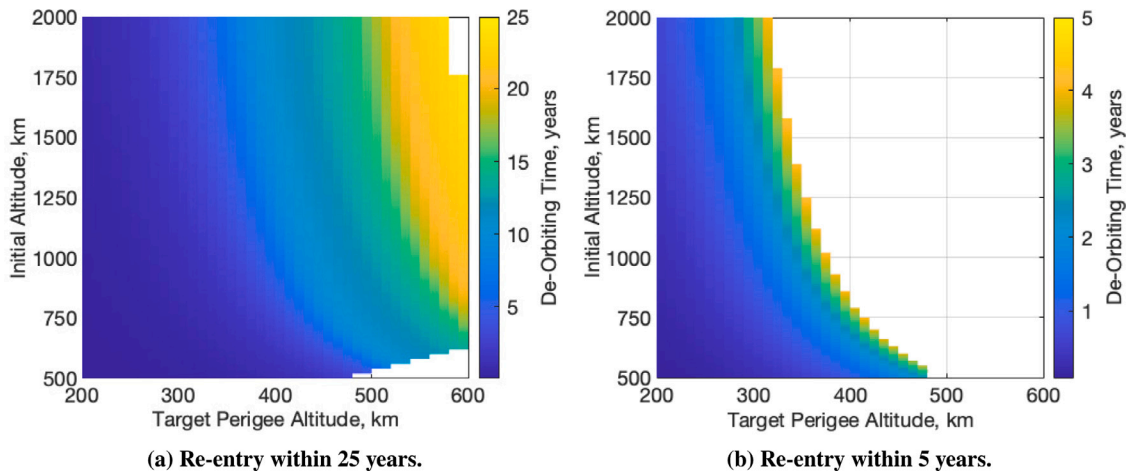

Fig. 9. ToF for the perigee decrease strategy.

(a) Re-entry within 25 years.

(b) Re-entry within 5 years.

Fig. 10. De-orbiting time for the perigee decrease strategy.

Table 11
Initial grids.

h_0, km	δh_0, km	i_0, deg	δi_0, deg	h_{tar}, km	δh_{tar}, km
[500, 2000]	10	[30, 120]	2	[200, 600]	10

5.2.2. De-orbiting mapping for perigee decrease strategy

Figs. 8 and 9 show the Δv-budget and ToF, respectively, required to move a spacecraft from given h_0 to h_{tar} for the perigee decrease strategy, where the white areas correspond to $h_0 \leq h_{tar}$. As shown in the maps, the lower the initial altitude and the higher the target perigee altitude, the smaller the Δv-budget and ToF will be; the ToF is proportional to the Δv-budget because the thrust is continuously applied.

Fig. 10 shows the de-orbiting time for the perigee decrease strategy, where the de-orbiting time accounts for the low-thrust transfer from given h_0 to h_{tar} and the passive de-orbiting from that h_{tar} until re-entry. In Figs. 9(a) and 9(b), the coloured areas denote the conditions in (h_0, h_{tar}) that can lead to re-entry within 25 and 5 years, respectively, where the requirement of 25 years is the guidance from the International-Agency Space Debris Coordination Committee for spacecraft in the LEO region and the requirement of 5 years is a guideline that has been considered by some large constellations (e.g., the Starlink constellation [47] and the OneWeb constellation [34]). Some conclusions are drawn from the maps.

(1) Generally, the lower the initial altitude and the lower the target perigee altitude, the faster the de-orbiting will be.
(2) If there is no limit on the Δv-budget, the perigee decrease strategy can achieve re-entry within 5 years from any initial altitudes up to 2000 km.

5.2.3. De-orbiting mapping for de-orbiting corridor strategy

Figs. 11 and 12 show the Δv-budget and ToF, respectively, required to move a spacecraft from a given (h_0, i_0) to the closest de-orbiting corridor for the de-orbiting corridor strategy, where the black curves indicate the location of the de-orbiting corridors, assuming $e = 0.001$. As shown in the maps, the closer the initial state to the corresponding target de-orbiting corridor, the smaller the Δv-budget and ToF will be; the ToF is proportional to the Δv-budget because the thrust is continuously applied.

Figs. 13 and 14 show the de-orbiting time for the de-orbiting corridor strategy, considering an area-to-mass ratio of 1 and 3 m²/kg, respectively, where the de-orbiting time accounts for the low-thrust transfer from a given (h_0, i_0) to the closest de-orbiting corridor and the passive de-orbiting from that de-orbiting corridor until re-entry.
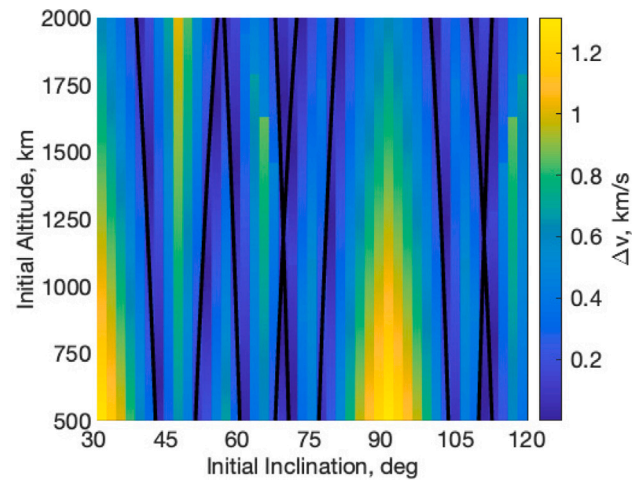

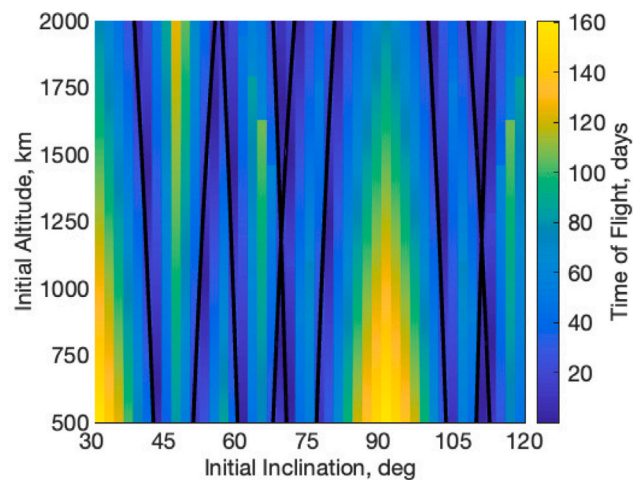**Fig. 11.** Δv-budget for the de-orbiting corridor strategy.

Fig. 12. ToF for the de-orbiting corridor strategy.

In Fig. 13(a), Figs. 13(b) and 13(c), Fig. 13(d), the coloured areas denote the conditions in (h_0, i_0) that can lead to re-entry within 25 and 5 years, respectively. Some conclusions are drawn from the maps.
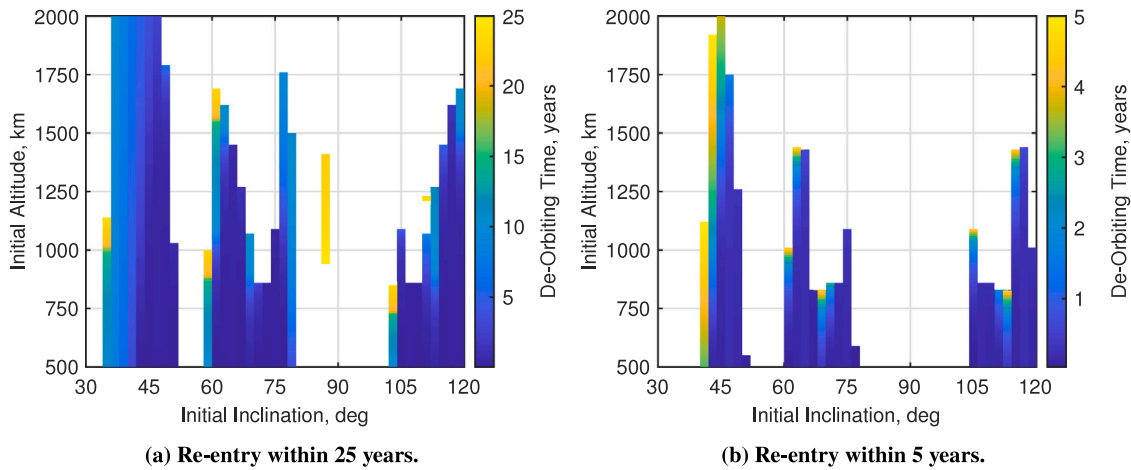
(a) Re-entry within 25 years.

(b) Re-entry within 5 years.

Fig. 13. De-orbiting time for the de-orbiting corridor strategy, for area-to-mass ratio = 1 m^2/kg.

(a) Re-entry within 25 years.

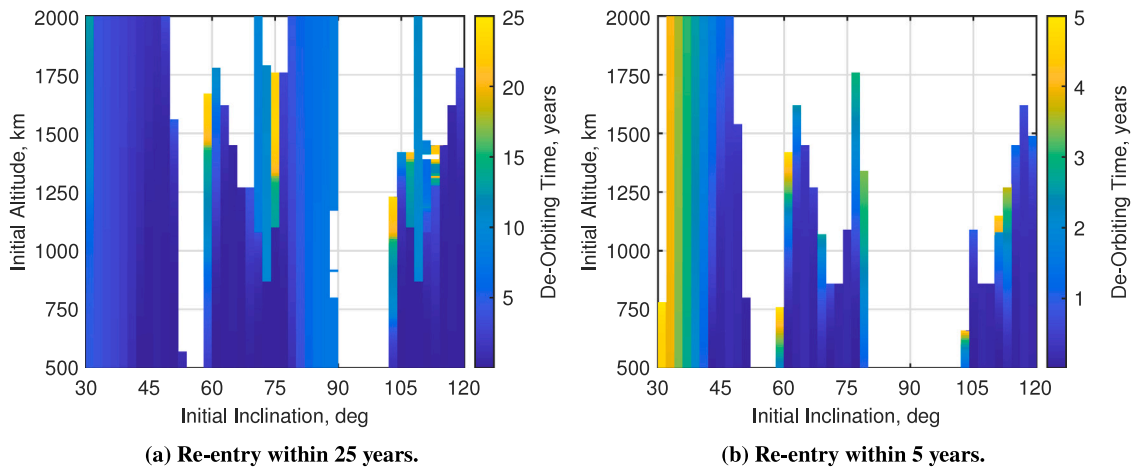(b) Re-entry within 5 years.

Fig. 14. De-orbiting time for the de-orbiting corridor strategy, for area-to-mass ratio = 3 m^2/kg.

(1) Among the six de-orbiting corridors, the de-orbiting corridor located at the inclination between 30 and 45 deg, which is specified by $n_1 = 1$, $n_2 = 1$, and $n_3 = -1$, is the most efficient one.

(2) Due to the fact that the passive de-orbiting device can act as a drag sail, the low and middle LEO altitudes show a relatively wider region for exploitable initial conditions [13].

(3) Generally, the ability of the de-orbiting corridor strategy depends on the area-to-mass ratio for a given target de-orbiting corridor; the larger the area-to-mass ratio, the faster the de-orbiting will be.

5.2.4. Comparison between de-orbiting strategies

Finally, we compare the Δv-budget between the two strategies to identify their respective feasible altitudes and inclinations for given de-orbiting time requirements (i.e., re-entry within 25 and 5 years), as shown in Figs. 15 and 16, where the area-to-mass ratios considered for the de-orbiting corridor strategy are 1 and 3 m^2/kg, respectively. In the maps, the green areas denote the initial altitudes and inclinations where the Δv-budgets by the de-orbiting corridor strategy are smaller than those by the perigee decrease strategy, and thus if de-orbiting from these initial conditions, the de-orbiting corridor strategy will be superior. Accordingly, the remaining blue areas denote the feasible altitudes and inclinations of the perigee decrease strategy. Note that for the perigee decrease strategy, the Δv-budget used in the comparison

is the minimum value to de-orbit from a given h_0 with a given de-orbiting time requirement (i.e., re-entry within 25 or 5 years), and this value is assumed identical for all initial inclinations, recalling that the initial inclination has ignorable influence on the results for the perigee decrease strategy.

As indicated in the maps, the de-orbiting corridor strategy spends more Δv-budget than the perigee decrease strategy in most of the LEO region because of the expensive inclination change; however, there still exist many cases, especially in the high-altitude LEO region, where the de-orbiting corridor strategy is more attractive. By reading the maps, the mission designers can choose their preferable strategy according to mission scenarios and requirements.

6. Conclusion

In this paper, two strategies exploiting the low-thrust and natural effects were investigated for the complete de-orbiting from LEO. For each strategy, a closed-loop steering law was designed with the Lyapunov method. By comparing against the time-optimal open-loop steering laws, the closed-loop steering laws proposed were demonstrated to be sub-optimal, thus making it possible to achieve fast re-entry. Besides, the steering laws have been proved to be stable, and thus they are robust to any initial condition in the LEO region. Then the averaged low-thrust EoMs were derived with the orbital averaging technique, and the numerical test has shown that the combination of the computational load and accuracy of the averaged EoMs renders them advantageous over the exact EoMs. By using the averaged low-thrust EoMs, a series of
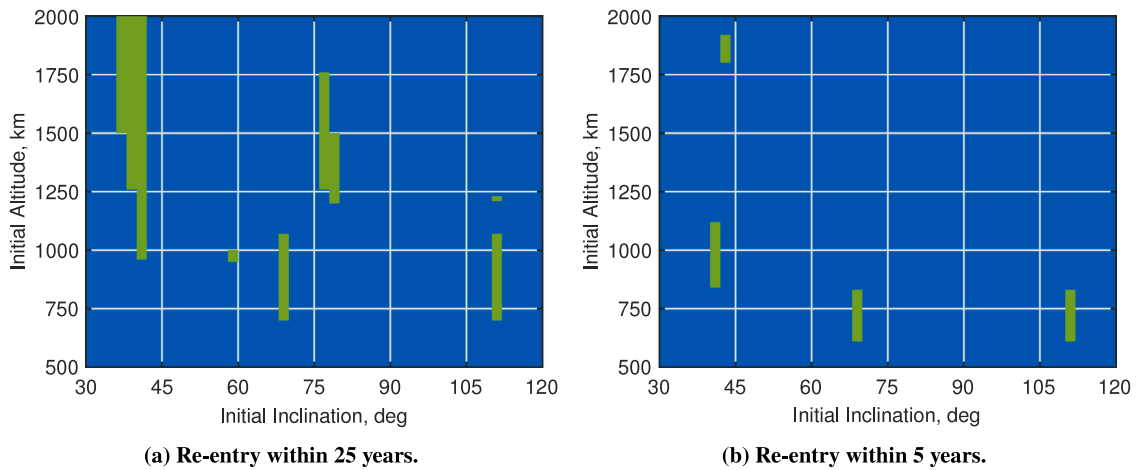
Fig. 15. Feasible altitudes and inclinations to apply the two strategies, for area-to-mass ratio = 1 m²/kg (green: Δv-budget by de-orbiting corridor strategy less than perigee decrease strategy, blue: Δv-budget by perigee decrease strategy less than de-orbiting corridor strategy). (For interpretation of the references to colour in this figure legend, the reader is referred to the web version of this article.)

Fig. 16. Feasible altitudes and inclinations to apply the two strategies, for area-to-mass ratio = 3 m²/kg (green: Δv-budget by de-orbiting corridor strategy less than perigee decrease strategy, blue: Δv-budget by perigee decrease strategy less than de-orbiting corridor strategy). (For interpretation of the references to colour in this figure legend, the reader is referred to the web version of this article.)
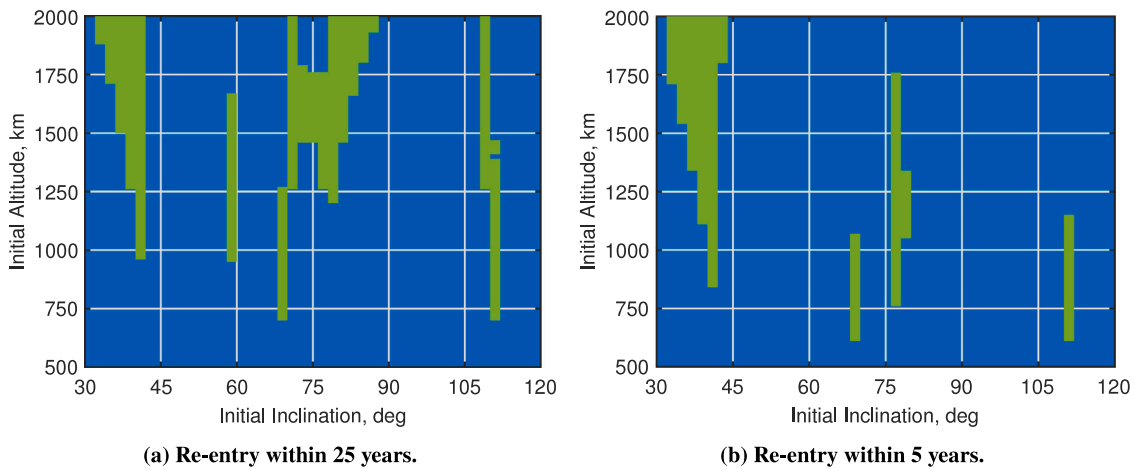
initial conditions over the entire LEO region were rapidly propagated, and subsequently, a set of maps was obtained, showing the Δv-budget and de-orbiting time for the de-orbiting from LEO for the two strategies. It is read from the maps that if there is no limit on the Δv-budget, the perigee decrease strategy is able to achieve re-entry within 5 years from any initial altitude up to 2000 km, while the ability of the de-orbiting corridor strategy depends on the initial altitude and inclination, as well as the area-to-mass ratio of the passive de-orbiting device. By comparing the Δv-budget, another set of maps was obtained, revealing the feasible altitude and inclination, which are key cost drivers, to apply the two strategies given the de-orbiting time requirements. It is read from the maps that mostly, the perigee decrease strategy is superior, because the de-orbiting corridor strategy is involved in an expensive inclination change; however, there still exist many cases, especially in the high-altitude LEO region, where the de-orbiting corridor strategy is more attractive.

Funding sources

Declaration of competing interest

The authors declare that they have no known competing financial interests or personal relationships that could have appeared to influence the work reported in this paper.

Acknowledgements

Appendix A. Expressions in Eq. (39)

The expressions of b_k^F and b_k^E ($k = 0$ to 4) that appear in Eq. (39) are given below.

$$b_0^F = 1 \tag{43a}$$

$$b_1^F = -\frac{2}{c_i^2}\left(2c_a^2 + c_i^2\right) \tag{43b}$$

$$b_2^F = \frac{2}{3c_i^4}\left(16c_a^4 + 16c_a^2 c_i^2 + 3c_i^4\right) \tag{43c}$$

$$b_3^F = -\frac{2}{15c_i^6}\left(256c_a^6 + 384c_a^4c_i^2 + 158c_a^2c_i^4 + 15c_i^6\right) \tag{43d}$$

$$b_4^F = \frac{2}{105c_i^8}\left(6144c_a^8 + 12288c_a^6c_i^2 + 8000c_a^4c_i^4 + 1856c_a^2c_i^6 + 105c_i^8\right) \tag{43e}$$

$$b_0^E = 0 \tag{44a}$$

$$b_1^E = \frac{4}{c_i^2}\left(c_a^2 + c_i^2\right) \tag{44b}$$

$$b_2^E = -\frac{16}{3c_i^4}\left(2c_a^4 + 3c_a^2c_i^2 + c_i^4\right) \tag{44c}$$

$$b_3^E = \frac{4}{15c_i^6}\left(128c_a^6 + 256c_a^4c_i^2 + 151c_a^2c_i^4 + 23c_i^6\right) \tag{44d}$$

$$b_4^E = -\frac{64}{105c_i^8}\left(192c_a^8 + 480c_a^6c_i^2 + 406c_a^4c_i^4 + 129c_a^2c_i^6 + 11c_i^8\right) \tag{44e}$$

The expressions of $\left(\mathrm{fun}_k\right)_x$ ($k = 0$ to 4 and $x \in (a,\ e,\ i,\ \Omega,\ \omega)$) that appear in Eq. (56) are given as follows.

$$\left(\mathrm{fun}_0\right)_a = 4E \tag{45a}$$

$$\left(\mathrm{fun}_1\right)_a = 2\sin\left(2\omega + 2E\right) \tag{45b}$$

$$\left(\mathrm{fun}_2\right)_a = \sin\left(4\omega + 4E\right) \tag{45c}$$

$$\left(\mathrm{fun}_3\right)_a = \frac{2}{3}\sin\left(6\omega + 6E\right) \tag{45d}$$

$$\left(\mathrm{fun}_4\right)_a = \frac{1}{2}\sin\left(8\omega + 8E\right) \tag{45e}$$

$$\left(\mathrm{fun}_0\right)_e = \frac{1}{2}\left(8\sin E - e\sin 2E - 6eE\right) \tag{46a}$$

$$\left(\mathrm{fun}_1\right)_e = \frac{1}{24}\left[48\sin\left(2\omega + E\right) - 36e\sin\left(2\omega + 2E\right)\right.$$
$$\left.+ 16\sin\left(2\omega + 3E\right) - 3e\sin\left(2\omega + 4E\right) - 12eE\cos 2\omega\right] \tag{46b}$$

$$\left(\mathrm{fun}_2\right)_e = \frac{1}{60}\left[-15e\sin\left(4\omega + 2E\right) + 40\sin\left(4\omega + 3E\right)\right.$$
$$\left.- 45e\sin\left(4\omega + 4E\right) + 24\sin\left(4\omega + 5E\right) - 5e\sin\left(4\omega + 6E\right)\right] \tag{46c}$$

$$\left(\mathrm{fun}_3\right)_e = \frac{1}{560}\left[-70e\sin\left(6\omega + 4E\right) + 224\sin\left(6\omega + 5E\right)\right.$$
$$\left.- 280e\sin\left(6\omega + 6E\right) + 160\sin\left(6\omega + 7E\right) - 35e\sin\left(6\omega + 8E\right)\right] \tag{46d}$$

$$\left(\mathrm{fun}_4\right)_e = \frac{1}{2520}\left[-210e\sin\left(8\omega + 6E\right) + 720\sin\left(8\omega + 7E\right)\right.$$
$$\left.- 945e\sin\left(8\omega + 8E\right) + 560\sin\left(8\omega + 9E\right) - 126e\sin\left(8\omega + 10E\right)\right] \tag{46e}$$

$$\left(\mathrm{fun}_0\right)_i = \frac{1}{12}\left[-3e\left(\frac{7}{\sqrt{1 - e^2}} + 1\right)\sin E + 3\left(\frac{1 + e^2}{\sqrt{1 - e^2}} - 1\right)\sin 2E\right.$$
$$- e\left(\frac{1}{\sqrt{1 - e^2}} - 1\right)\sin 3E + 3e\left(\frac{1}{\sqrt{1 - e^2}} - 1\right)\sin\left(2\omega - E\right)$$
$$- \frac{18e}{\sqrt{1 - e^2}}\sin\left(2\omega + E\right) + 3\left(\frac{1 + e^2}{\sqrt{1 - e^2}} + 1\right)\sin\left(2\omega + 2E\right)$$
$$- e\left(\frac{1}{\sqrt{1 - e^2}} + 1\right)\sin\left(2\omega + 3E\right) + 6\left(\frac{1 + e^2}{\sqrt{1 - e^2}} + 1\right)E$$
$$\left.+ 6\left(\frac{1 + e^2}{\sqrt{1 - e^2}} - 1\right)E\cos 2\omega\right] \tag{47a}$$

$$\left(\mathrm{fun}_2\right)_i = \frac{1}{840}\left\{\left[210e\cos\left(3\omega + E\right) - 210\cos\left(3\omega + 2E\right)\right.\right.$$
$$+ 105\cos\left(3\omega + 4E\right) - 42e\cos\left(3\omega + 5E\right)$$
$$+ 70e\cos\left(5\omega + 3E\right) - 105\cos\left(5\omega + 4E\right)$$
$$\left.+ 70\cos\left(5\omega + 6E\right) - 30e\cos\left(5\omega + 7E\right)\right]\sin\omega$$
$$+ \left[-210e\sin\left(3\omega + E\right) + 210\left(1 + e^2\right)\sin\left(3\omega + 2E\right)\right.$$
$$+ 105\left(1 + e^2\right)\sin\left(3\omega + 4E\right) - 42e\sin\left(3\omega + 5E\right)$$
$$- 70e\sin\left(5\omega + 3E\right) + 105\left(1 + e^2\right)\sin\left(5\omega + 4E\right)$$
$$+ 70\left(1 + e^2\right)\sin\left(5\omega + 6E\right) - 30e\sin\left(5\omega + 7E\right)$$
$$\left.\left.- 420e\sin\left(3\omega + 3E\right) - 252e\sin\left(5\omega + 5E\right)\right]\frac{\cos\omega}{\sqrt{1 - e^2}}\right\} \tag{47b}$$

$$\left(\mathrm{fun}_3\right)_i = \frac{1}{5040}\left\{\left[420e\cos\left(5\omega + 3E\right) - 630\cos\left(5\omega + 4E\right)\right.\right.$$
$$+ 420\cos\left(5\omega + 6E\right) - 180e\cos\left(5\omega + 7E\right)$$
$$+ 252e\cos\left(7\omega + 5E\right) - 420\cos\left(7\omega + 6E\right)$$
$$\left.+ 315\cos\left(7\omega + 8E\right) - 140e\cos\left(7\omega + 9E\right)\right]\sin\omega$$
$$+ \left[-420e\sin\left(5\omega + 3E\right) + 630\left(1 + e^2\right)\sin\left(5\omega + 4E\right)\right.$$
$$+ 420\left(1 + e^2\right)\sin\left(5\omega + 6E\right) - 180e\sin\left(5\omega + 7E\right)$$
$$- 252e\sin\left(7\omega + 5E\right) + 420\left(1 + e^2\right)\sin\left(7\omega + 6E\right)$$
$$+ 315\left(1 + e^2\right)\sin\left(7\omega + 8E\right) - 140e\sin\left(7\omega + 9E\right)$$
$$\left.\left.- 1512e\sin\left(5\omega + 5E\right) - 1080e\sin\left(7\omega + 7E\right)\right]\frac{\cos\omega}{\sqrt{1 - e^2}}\right\} \tag{47c}$$

$$\left(\mathrm{fun}_4\right)_i = \frac{1}{55440}\left\{\left[2772e\cos\left(7\omega + 5E\right) - 4620\cos\left(7\omega + 6E\right)\right.\right.$$
$$+ 3465\cos\left(7\omega + 8E\right) - 1540e\cos\left(7\omega + 9E\right)$$
$$+ 1980e\cos\left(9\omega + 7E\right) - 3465\cos\left(9\omega + 8E\right)$$
$$\left.+ 2772\cos\left(9\omega + 10E\right) - 1260e\cos\left(9\omega + 11E\right)\right]\sin\omega$$
$$+ \left[-2772e\sin\left(7\omega + 5E\right) + 4620\left(1 + e^2\right)\sin\left(7\omega + 6E\right)\right.$$
$$+ 3465\left(1 + e^2\right)\sin\left(7\omega + 8E\right) - 1540e\sin\left(7\omega + 9E\right)$$
$$- 1980e\sin\left(9\omega + 7E\right) + 3465\left(1 + e^2\right)\sin\left(9\omega + 8E\right)$$
$$+ 2772\left(1 + e^2\right)\sin\left(9\omega + 10E\right) - 1260e\sin\left(9\omega + 11E\right)$$
$$\left.\left.- 11880e\sin\left(7\omega + 7E\right) - 9240e\sin\left(9\omega + 9E\right)\right]\frac{\cos\omega}{\sqrt{1 - e^2}}\right\} \tag{47d}$$

$$\left(\mathrm{fun}_0\right)_\Omega = \frac{1}{12}\left[-3e\left(\frac{5}{\sqrt{1 - e^2}} - 1\right)\cos E + 3\left(\frac{1 + e^2}{\sqrt{1 - e^2}} - 1\right)\cos 2E\right.$$
$$- e\left(\frac{1}{\sqrt{1 - e^2}} - 1\right)\cos 3E - 3e\left(\frac{1}{\sqrt{1 - e^2}} - 1\right)\cos\left(2\omega - E\right)$$
$$+ \frac{18e}{\sqrt{1 - e^2}}\cos\left(2\omega + E\right) - 3\left(\frac{1 + e^2}{\sqrt{1 - e^2}} + 1\right)\cos\left(2\omega + 2E\right)$$
$$\left.+ e\left(\frac{1}{\sqrt{1 - e^2}} + 1\right)\cos\left(2\omega + 3E\right) + 6\left(\frac{1 + e^2}{\sqrt{1 - e^2}} - 1\right)E\sin 2\omega\right] \tag{48a}$$

$$\left(\mathrm{fun}_1\right)_\Omega = \frac{1}{120}\left\{\left[30e\cos\left(\omega - E\right) - 30\cos\left(\omega + 2E\right) + 10e\cos\left(\omega + 3E\right)\right.\right.$$
$$- 30e\cos\left(3\omega + E\right) + 30\cos\left(3\omega + 2E\right) - 15\cos\left(3\omega + 4E\right)$$
$$\left.+ 6e\cos\left(3\omega + 5E\right)\right]\cos\omega + \left[30e\sin\left(\omega - E\right)\right.$$
$$+ 30\left(1 + e^2\right)\sin\left(\omega + 2E\right) - 10e\sin\left(\omega + 3E\right)$$
$$- 30e\sin\left(3\omega + E\right) + 30\left(1 + e^2\right)\sin\left(3\omega + 2E\right)$$
$$+ 15\left(1 + e^2\right)\sin\left(3\omega + 4E\right) - 6e\sin\left(3\omega + 5E\right)$$
$$\left.- 180e\sin\left(\omega + E\right) - 60e\sin\left(3\omega + 3E\right)\right]\frac{\sin\omega}{\sqrt{1 - e^2}}$$
$$\left.+ 30\left(\frac{1 + e^2}{\sqrt{1 - e^2}} - 1\right)E\sin 2\omega\right\} \tag{48b}$$

$$(\text{fun}_2)_\Omega = \frac{1}{840}\{[-210e\cos(3\omega+E)+210\cos(3\omega+2E)$$
$$-105\cos(3\omega+4E)+42e\cos(3\omega+5E)$$
$$-70e\cos(5\omega+3E)+105\cos(5\omega+4E)$$
$$-70\cos(5\omega+6E)+30e\cos(5\omega+7E)]\cos\omega$$
$$+[-210e\sin(3\omega+E)+210(1+e^2)\sin(3\omega+2E)$$
$$+105(1+e^2)\sin(3\omega+4E)-42e\sin(3\omega+5E)$$
$$-70e\sin(5\omega+3E)+105(1+e^2)\sin(5\omega+4E)$$
$$+70(1+e^2)\sin(5\omega+6E)-30e\sin(5\omega+7E)$$
$$-420e\sin(3\omega+3E)-252e\sin(5\omega+5E)]\frac{\sin\omega}{\sqrt{1-e^2}}\} \quad (48c)$$

$$(\text{fun}_3)_\Omega = \frac{1}{5040}\{[-420e\cos(5\omega+3E)+630\cos(5\omega+4E)$$
$$-420\cos(5\omega+6E)+180e\cos(5\omega+7E)$$
$$-252e\cos(7\omega+5E)+420\cos(7\omega+6E)$$
$$-315\cos(7\omega+8E)+140e\cos(7\omega+9E)]\cos\omega$$
$$+[-420e\sin(5\omega+3E)+630(1+e^2)\sin(5\omega+4E)$$
$$+420(1+e^2)\sin(5\omega+6E)-180e\sin(5\omega+7E)$$
$$-252e\sin(7\omega+5E)+420(1+e^2)\sin(7\omega+6E)$$
$$+315(1+e^2)\sin(7\omega+8E)-140e\sin(7\omega+9E)$$
$$-1512e\sin(5\omega+5E)-1080e\sin(7\omega+7E)]\frac{\sin\omega}{\sqrt{1-e^2}}\} \quad (48d)$$

$$(\text{fun}_4)_\Omega = \frac{1}{55440}\{[-2772e\cos(7\omega+5E)+4620\cos(7\omega+6E)$$
$$-3465\cos(7\omega+8E)+1540e\cos(7\omega+9E)$$
$$-1980e\cos(9\omega+7E)+3465\cos(9\omega+8E)$$
$$-2772\cos(9\omega+10E)+1260e\cos(9\omega+11E)]\cos\omega$$
$$+[-2772e\sin(7\omega+5E)+4620(1+e^2)\sin(7\omega+6E)$$
$$+3465(1+e^2)\sin(7\omega+8E)-1540e\sin(7\omega+9E)$$
$$-1980e\sin(9\omega+7E)+3465(1+e^2)\sin(9\omega+8E)$$
$$+2772(1+e^2)\sin(9\omega+10E)-1260e\sin(9\omega+11E)$$
$$-11880e\sin(7\omega+7E)-9240e\sin(9\omega+9E)]\frac{\sin\omega}{\sqrt{1-e^2}}\} \quad (48e)$$

$$(\text{fun}_0)_\omega = [-2(2-e^2)\cos E + e\cos^2 E] \quad (49a)$$

$$(\text{fun}_1)_\omega = \frac{1}{24}[24(2-e^2)\cos(2\omega+E)-8(2-e^2)\cos(2\omega+3E)$$
$$+3e\cos(2\omega+4E)+12eE\sin 2\omega] \quad (49b)$$

$$(\text{fun}_2)_\omega = \frac{1}{60}[-15e\cos(4\omega+2E)+20(2-e^2)\cos(4\omega+3E)$$
$$-12(2-e^2)\cos(4\omega+5E)+5e\cos(4\omega+6E)] \quad (49c)$$

$$(\text{fun}_3)_\omega = \frac{1}{560}[-70e\cos(6\omega+4E)+112(2-e^2)\cos(6\omega+5E)$$
$$-80(2-e^2)\cos(6\omega+7E)+35e\cos(6\omega+8E)] \quad (49d)$$

$$(\text{fun}_4)_\omega = \frac{1}{1260}[-105e\cos(8\omega+6E)+180(2-e^2)\cos(8\omega+7E)$$
$$-140(2-e^2)\cos(8\omega+9E)+63e\cos(8\omega+10E)] \quad (49e)$$

Appendix B. Time-optimal open-loop control law design

The time-optimal open-loop control law design is presented in this section.

The equations of motion due to low-thrust and J_2-effect can be stated as

$$\dot{x} = g(x,\hat{f}) = A(x)\hat{f} + b(x) \quad (50)$$

where $x = \{a,e,i,\Omega,\omega,E,m\}^\top$ is the vector of state variables; $\hat{f} = \{\hat{f}_r,\hat{f}_\theta,\hat{f}_h\}^\top$ is the vector of control variables, which in the current problem is the unit vector of the low-thrust acceleration, i.e. the thrust direction; the matrix A and the vector b are functions of x.

The minimum-time low-thrust transfer problem is formulated as follows. Find the optimal control $\hat{f}^*$ that minimises

$$J = \int_{t_0}^{t_f} dt \quad (51)$$

with the initial condition

$$x\big|_{t=t_0} = x_0 \quad (52)$$

and the terminal condition

$$\psi(x)\big|_{t=t_f} = 0 \quad (53)$$

where the terminal conditions for the two strategies have been given in Eqs. (10) and (19).

The Hamiltonian function for a minimum-time problem reads [42]

$$H = 1 + \lambda^\top \dot{x} = 1 + \lambda^\top(A\hat{f}+b) \quad (54)$$

where $\lambda = \{\lambda_a,\lambda_e,\lambda_i,\lambda_\Omega,\lambda\omega,\lambda_E,\lambda_m\}^\top$ is the vector of costates.

The optimal solutions $(x^*,\lambda^*,\hat{f}^*)$ satisfy the Euler–Lagrange equations [42]

$$\dot{x} = H_\lambda \quad (55a)$$

$$\dot{\lambda} = -H_x \quad (55b)$$

along with the transversality conditions [42]

$$\Psi(y)\big|_{t=t_f} = \begin{Bmatrix} H \\ \lambda - \upsilon\psi_x \\ \psi \end{Bmatrix}_{t=t_f} = 0 \quad (56)$$

where y denotes the vector consisting of the states and costates, and υ is the terminal multiplier, which can be eliminated by hand in the current problem. For the two strategies, $\Psi(y)$ can be separately reduced to

$$\Psi^{\text{str1}}(y) = \begin{Bmatrix} 1 + \lambda_a\dot{a} + \lambda_e\dot{e} \\ \lambda_a a + \lambda_e(1-e) \\ \lambda_i \\ \lambda_\Omega \\ \lambda_\omega \\ \lambda_E \\ \lambda_m \\ a(1-e) - (h_{pf}+R_\oplus) \end{Bmatrix} \quad (57)$$

$$\Psi^{\text{str2}}(y) = \begin{Bmatrix} 1 + \lambda_a\dot{a} + \lambda_e\dot{e} + \lambda_i i \\ 8\lambda_a ae + 7\lambda_e(1-e^2) \\ 2\lambda_a a(2n_1\sin i - 5n_2\sin 2i) + 7\lambda_i(5n_2\cos^2 i - 2n_1\cos i - n_2) \\ \lambda_\Omega \\ \lambda_\omega \\ \lambda_E \\ \lambda_m \\ \frac{3\sqrt{\mu}J_2 R_\oplus^2}{4a^{7/2}(1-e^2)^2}(5n_2\cos^2 i - 2n_1\cos i - n_2) + n_3 n_S \end{Bmatrix} \quad (58)$$

According to the Pontryagin Minimum Principle [48], the optimal thrust direction that minimises H is anti-parallel to $A^\top\lambda$:

$$\hat{f}^* = -\frac{A^\top\lambda}{\|A^\top\lambda\|} \quad (59)$$

with which, the dynamics including both the states and costates becomes

$$\dot{y} = G(y) \quad \Rightarrow \quad \begin{Bmatrix} \dot{x} \\ \dot{\lambda} \end{Bmatrix} = \begin{Bmatrix} -\frac{AA^\top\lambda}{\|A^\top\lambda\|}+b \\ \dfrac{\partial\left(\frac{\lambda^\top AA^\top\lambda}{\|A^\top\lambda\|}-\lambda^\top b\right)}{\partial x} \end{Bmatrix} \quad (60)$$

Now the minimum-time problem has been converted to a Two-Point Boundary Value Problem (TPBVP), stated as follows. Find (λ_0,t_f) such that $y(t)$, which is subject to Eq. (60), satisfies Eq. (56) at $t=t_f$. There are various methods to solve a TPBVP, such as the typical shooting

method and the Newton method combined with the Particle Swarm Optimisation algorithm [49]. In this work we solve the TPBVP by means of the shooting method.

In order to increase the accuracy and robustness of the shooting procedure, the state transition matrix

$$\boldsymbol{\Phi}(t_0,\, t) = \partial \boldsymbol{y}(t)/\partial \boldsymbol{y}(t_0), \quad \boldsymbol{\Phi}(t_0,\, t_0) = \boldsymbol{I}_{14\times14} \tag{61}$$

which maps the variations in states $\delta \boldsymbol{y}(t)$ with respect to the variations in initial conditions $\delta \boldsymbol{y}(t_0)$ over $t_0 \to t$, i.e., $\delta \boldsymbol{y}(t) = \boldsymbol{\Phi}(t_0,\, t)\,\delta \boldsymbol{y}(t_0)$, is provided [50]. The time derivative of $\boldsymbol{\Phi}(t_0,\, t)$ is given by

$$\dot{\boldsymbol{\Phi}}(t_0,\, t) = \boldsymbol{J}\boldsymbol{\Phi}(t_0,\, t) \tag{62}$$

where $\boldsymbol{J}$ is the Jacobian of $\boldsymbol{G}(\boldsymbol{y})$.

Eq. (62) contains 196 differential equations which are required to be evaluated along $\boldsymbol{y}(t)$. Let $\boldsymbol{z}$ denotes the vector consisting of the elements in $\boldsymbol{y}$ and $\boldsymbol{\Phi}$. The integrated dynamics is

$$\dot{\boldsymbol{z}} = \mathcal{G}(\boldsymbol{z}) \quad \Rightarrow \quad \left\{ \begin{array}{c} \dot{\boldsymbol{y}} \\ \mathrm{vec}(\dot{\boldsymbol{\Phi}}) \end{array} \right\} = \left\{ \begin{array}{c} \boldsymbol{G}(\boldsymbol{y}) \\ \mathrm{vec}(\boldsymbol{J}\boldsymbol{\Phi}) \end{array} \right\} \tag{63}$$

Besides, to eliminate dependence on a specific central attracting body and to allow global mapping of solutions [33, p. 363], the time and distance units are scaled as

$$1\ \mathrm{TU} = \sqrt{R_\oplus^3/\mu}, \quad 1\ \mathrm{DU} = R_\oplus \tag{64}$$

References

[1] B.B. Virgili, J.C. Dolado, H.G. Lewis, et al., Risk to space sustainability from large constellations of satellites, Acta Astronaut. 126 (2016) 154–162, http://dx.doi.org/10.1016/j.actaastro.2016.03.034, September–October.

[2] J.E. Pollard, Evaluation of low-thrust orbital maneuvers, in: 34th AIAA/ASME/SAE/ASEE Joint Propulsion Conference and Exhibit, Cleveland, Ohio, United States of America, 1998, http://dx.doi.org/10.2514/6.1998-3486, 13-15 July.

[3] G. Mengali, A.A. Quarta, Solar sail trajectories with piecewise-constant steering laws, Aerosp. Sci. Technol. 13 (8) (2009) 431–441, http://dx.doi.org/10.1016/j.ast.2009.06.007, December.

[4] L. Niccolai, A.A. Quarta, G. Mengali, Analytical solution of the optimal steering law for non-ideal solar sail, Aerosp. Sci. Technol. 62 (2017) 11–18, March.

[5] L. Niccolai, A.A. Quarta, G. Mengali, Solar sail trajectory analysis with asymptotic expansion method, Aerosp. Sci. Technol. 68 (2017) 431–440, http://dx.doi.org/10.1016/j.ast.2017.05.038, September.

[6] A. Caruso, A.A. Quarta, G. Mengali, M. Ceriotti, Shape-based approach for solar sail trajectory optimization, Aerosp. Sci. Technol. 107 (2020) 106363, http://dx.doi.org/10.1016/j.ast.2020.106363, December.

[7] C. Lücking, C. Colombo, C.R. McInnes, A passive satellite deorbiting strategy for medium earth orbit using solar radiation pressure and the J_2 effect, Acta Astronaut. 77 (2012) 197–206, http://dx.doi.org/10.1016/j.actaastro.2012.03.026, August–September.

[8] C. Colombo, C. Lücking, C.R. McInnes, Orbital dynamics of high area-to-mass ratio spacecraft with J_2 and solar radiation pressure for novel earth observation and communication services, Acta Astronaut. 81 (1) (2012) 137–150, http://dx.doi.org/10.1016/j.actaastro.2012.07.009, December.

[9] C. Lücking, C. Colombo, C.R. McInnes, Solar radiation pressure-augmented deorbiting: Passive end-of-life disposal from high-altitude orbits, J. Spacecr. Rockets 50 (6) (2013) 1256–1267, http://dx.doi.org/10.2514/1.A32478, November.

[10] C. Colombo, T.d.B. De Fer, Assessment of passive and active solar sailing strategies for end-of-life re-entry, in: 67th International Astronautical Congress, Guadalajara, Mexico, 2016, 26-30 September, IAC-16-A6.4.4.

[11] E.M. Alessi, G. Schettino, A. Rossi, G.B. Valsecchi, Solar radiation pressure resonances in low earth orbits, Mon. Not. R. Astron. Soc. 473 (2) (2018) 2407–2414, http://dx.doi.org/10.1093/mnras/stx2507, January.

[12] G. Schettino, E.M. Alessi, A. Rossi, G.B. Valsecchi, Exploiting dynamical perturbations for the end-of-life disposal of spacecraft in LEO, Astron. Comput. 27 (2019) 1–10, http://dx.doi.org/10.1016/j.ascom.2019.02.001, April.

[13] A. Rossi, E.M. Alessi, G. Schettino, V. Schaus, G.B. Valsecchi, How an aware usage of the long-term dynamics can improve the long-term situation in the LEO region, Acta Astronaut. 174 (2020) 159–165, http://dx.doi.org/10.1016/j.actaastro.2020.05.005, September.

[14] O. von Stryk, R. Bulirsch, Direct and indirect methods for trajectory optimization, Ann. Oper. Res. 37 (1992) 357–373, http://dx.doi.org/10.1007/BF02071065, December.

[15] J.T. Betts, Survey of numerical methods for trajectory optimization, J. Guid. Control Dyn. 21 (2) (1998) 193–207, http://dx.doi.org/10.2514/2.4231, March.

[16] A.E. Petropoulos, Low-thrust orbit transfers using candidate Lyapunov functions with a mechanism for coasting, in: AIAA/AAS Astrodynamics Specialist Conference and Exhibit, Providence, Rhode Island, United States of America, 2004, http://dx.doi.org/10.2514/6.2004-5089, 16-19 August.

[17] D.B. Spencer, R.D. Culp, Designing continuous-thrust low-earth-orbit to geosynchronous-earth-orbit transfers, J. Spacecr. Rockets 32 (6) (1995) 1033–1038, http://dx.doi.org/10.2514/3.26726, November.

[18] C.A. Kluever, S.R. Oleson, Direct approach for computing near-optimal low-thrust earth-orbit transfers, J. Spacecr. Rockets 35 (4) (1998) 509–515, http://dx.doi.org/10.2514/2.3360, July.

[19] C.A. Kluever, Simple guidance scheme for low-thrust orbit transfers, J. Guid. Control Dyn. 21 (6) (1998) 1015–1017, http://dx.doi.org/10.2514/2.4344, November.

[20] C.A. Kluever, D.J. O'Shaughnessy, Trajectory-tracking guidance law for low-thrust earth-orbit transfers, J. Guid. Control Dyn. 23 (4) (2000) 754–756, http://dx.doi.org/10.2514/2.4597, July.

[21] Y. Gao, Near-optimal very low-thrust earth-orbit transfers and guidance schemes, J. Guid. Control Dyn. 30 (2) (2007) 529–539, http://dx.doi.org/10.2514/1.24836, March.

[22] A.E. Petropoulos, Simple control laws for low-thrust orbit transfers, in: AAS/AIAA Astrodynamics Specialist Conference, Big Sky, Montana, United States of America, 2003, 3-7 August, AAS 03-630.

[23] S. Hernandez, M.R. Akella, Lyapunov-based guidance for orbit transfers and rendezvous in levi-civita coordinates, J. Guid. Control Dyn. 37 (4) (2014) 1170–1181, http://dx.doi.org/10.2514/1.62305, July.

[24] Y. Gao, X. Li, Optimization of low-thrust many-revolution transfers and Lyapunov-based guidance, Acta Astronaut. 66 (1–2) (2010) 117–129, http://dx.doi.org/10.1016/j.actaastro.2009.05.013, January–February.

[25] M. Pontani, B. Conway, Optimal low-thrust orbital maneuvers via indirect swarming method, J. Optim. Theory Appl. 162 (2014) 272–292, http://dx.doi.org/10.1007/s10957-013-0471-9, July.

[26] D. Yang, B. Xu, Y. Gao, Optimal strategy for low-thrust spiral trajectories using Lyapunov-based guidance, Adv. Space Res. 56 (5) (2015) 865–878, http://dx.doi.org/10.1016/j.asr.2015.05.030, September.

[27] A. Ruggiero, P. Pergola, S. Marcuccio, M. Andrenucci, Low-thrust maneuvers for the efficient correction of orbital elements, in: 32nd International Electric Propulsion Conference, Wiesbaden, Germany, 2011, 11-15 September, IEPC-2011-102.

[28] S. Huang, C. Colombo, F. Bernelli-Zazzera, Low-thrust planar transfer for co-planar low earth orbit satellites considering self-induced collision avoidance, Aerosp. Sci. Technol. 106 (2020) 106198, http://dx.doi.org/10.1016/j.ast.2020.106198, November.

[29] L. Zhang, B. Xu, M. Li, F. Zhang, Semi-analytical approach for computing near-optimal low-thrust transfers to geosynchronous orbit, Aerosp. Sci. Technol. 55 (2016) 482–493, http://dx.doi.org/10.1016/j.ast.2016.06.022, August.

[30] E.M. Alessi, G. Schettino, A. Rossi, G.B. Valsecchi, Natural highways for end-of-life solutions in the LEO region, Celestial Mech. Dynam. Astronom. 130 (34) (2018) http://dx.doi.org/10.1007/s10569-018-9822-z, April.

[31] E.M. Alessi, C. Colombo, A. Rossi, Phase space description of the dynamics due to the coupled effect of the planetary oblateness and the solar radiation pressure perturbations, Celestial Mech. Dynam. Astronom. 131 (43) (2019) http://dx.doi.org/10.1007/s10569-019-9919-z, September.

[32] I. Gkolias, E. Alessi, C. Colombo, Dynamical taxonomy of the coupled solar radiation pressure and oblateness problem and analytical deorbiting configurations, Celestial Mech. Dynam. Astronom. 132 (55) (2020) http://dx.doi.org/10.1007/s10569-020-09992-2, November.

[33] D.A. Vallado (Ed.), Fundamentals of Astrodynamics and Applications, second ed., Microcosm Press and Kluwer Academic Publishers, 2004.

[34] https://www.oneweb.world/. Retrieved: 11 August, 2020.

[35] S. Huang, Multi-Phase Mission Analysis and Design of Satellite Constellations with Low-Thrust Propulsion (Ph.D. thesis), Politecnico di Milano, 2021, https://www.politesi.polimi.it/handle/10589/169779.

[36] J.E. Pollard, Simplified approach for assessment of low-thrust elliptical orbit transfers, in: 25th International Electric Propulsion Conference, Cleveland, Ohio, United States of America, 1997, pp. 979–986, 24-28 August, IEPC-97-160.

[37] J.P. Marec, Optimal Space Trajectories, Elsevier, 1979.

[38] T.N. Edelbaum, Propulsion requirements for controllable satellites, ARS J. 31 (8) (1961) 1079–1089, http://dx.doi.org/10.2514/8.5723.

[39] Y. Gao, C.A. Kluever, Analytic orbital averaging technique for computing tangential-thrust trajectories, J. Guid. Control Dyn. 28 (6) (2005) 1320–1323, http://dx.doi.org/10.2514/1.14698, November.

[40] J.A. Kechichian, Orbit raising with low-thrust tangential acceleration in presence of earth shadow, J. Spacecr. Rockets 35 (4) (1998) 516–525, http://dx.doi.org/10.2514/2.3361, July.

[41] R.H. Battin, An Introduction to the Mathematics and Methods of Astrodynamics, revised ed., American Institute of Aeronautics and Astronautics, 1999.

[42] A. Bryson, Y. Ho, Applied Optimal Control, Wiley, New York, 1975.

[43] F. Letterio, E.M. Alessi, I. Gkolias, et al., ReDSHIFT software tool for the design and computation of mission end-of-life disposal, in: 7th International Conference on Astrodynamics Tools and Techniques, DLR Oberpfaffenhofen, Germany, 2018, 6-8 November, http://redshift-h2020.eu/wp-content/uploads/2019/01/ICATT-7-2018-ReDSHIFT.pdf,

[44] C. Colombo, G. Vicario de Miguel, D.K. Skoulidou, N. Miguel Banos, E.M. Alessi, I. Gkolias, L. Carzana, F. Letterio, G. Schettino, K. Tsiganis, et al., ReDSHIFT disposal module for the design of end-of-life disposal trajectories for LEO to GEO missions, in: 70th International Astronautical Congress, Washington D.C., United States of America, 2019, 21-25 October, IAC-19, A6, 6, 4, x5370.

[45] V. Schaus, E.M. Alessi, G. Schettino, A. Rossi, E. Stoll, On the practical exploitation of perturbative effects in low earth orbit for space debris mitigation, Adv. Space Res. 63 (7) (2019) 1979–1991, http://dx.doi.org/10.1016/j.asr.2019.01.020.

[46] C. Colombo, I. Gkolias, Analysis of orbit stability in the geosynchronous region for end-of-life disposal, in: 7th European Conference on Space Debris, Darmstadt, Germany, 2017, 18-21 April, http://redshift-h2020.eu/wp-content/uploads/2018/03/1-Colombo-Gkolias-SpaceDebrisConf2017.pdf,

[47] https://www.starlink.com/. Retrieved: 11 August, 2020.

[48] L.S. Pontryagin, V.G. Boltyanskii, R.V. Gamkrelidze, E.F. Mishenko, Mathematical Theory of Optimal Processes, Wiley (Interscience), New York, 1962.

[49] D. Ye, M. Shi, Z. Sun, Satellite proximate pursuit-evasion game with different thrust configurations, Aerosp. Sci. Technol. 99 (2020) 105715, http://dx.doi.org/10.1016/j.ast.2020.105715.

[50] C. Zhang, F. Topputo, F. Bernelli-Zazzera, Y. Zhao, Low-thrust minimum-fuel optimization in the circular restricted three-body problem, J. Guid. Control Dyn. 38 (8) (2015) 1510, http://dx.doi.org/10.2514/1.G001080.